Since January 2020 Elsevier has created a COVID-19 resource centre with free information in English and Mandarin on the novel coronavirus COVID-19. The COVID-19 resource centre is hosted on Elsevier Connect, the company's public news and information website.

Cell Reports

Article

Structural basis and mode of action for two broadly neutralizing antibodies against SARS-CoV-2 emerging variants of concern

Graphical abstract

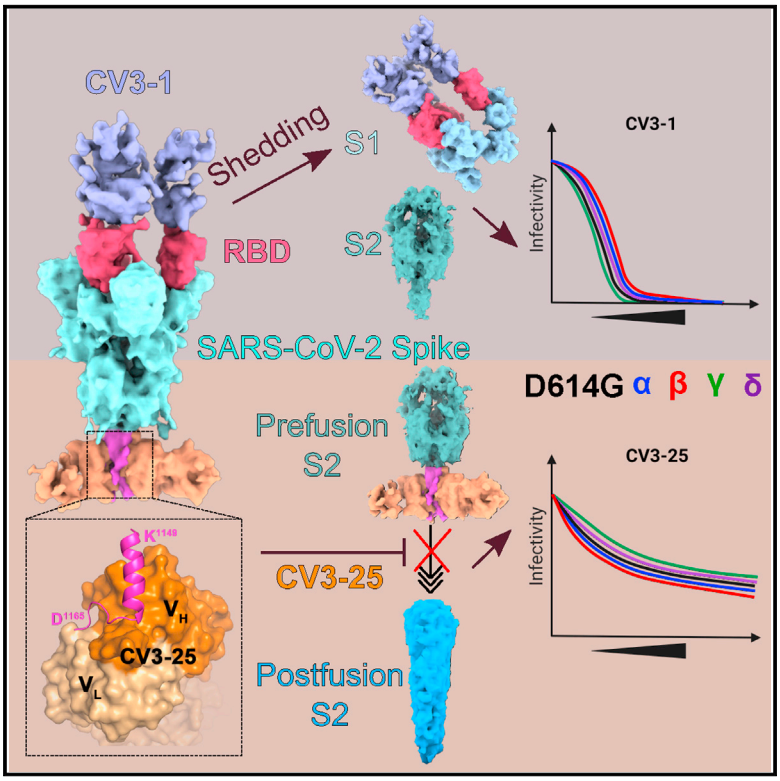

Highlights

- Antibodies CV3-1 and CV3-25 neutralize emerging SARS-CoV-2 variants
- CV3-1 binds to 485-GFN-487 loop of RBD on S and triggers S1 shedding
- CV3-25 binds the stem helix of S2 and inhibits membrane fusion
- Conserved epitopes are candidates for pan-coronavirus vaccines

Authors

Wenwei Li, Yaozong Chen, Jérémie Prévost, ..., Marzena Pazgier, Andrés Finzi, Walther Mothes

Correspondence

marzena.pazgier@usuhs.edu (M.P.), andres.finzi@umontreal.ca (A.F.), walther.mothes@yale.edu (W.M.)

In brief

Li et al. elucidate the structural basis and mode of action for two potent anti-S neutralizing monoclonal antibodies that remain effective against SARS-CoV-2 emerging variants of concern. Vaccine immunogen designs based on both conserved epitopes are candidates to elicit pan-coronavirus protective immune responses

Li et al., 2022, Cell Reports *38*, 110210
January 11, 2022
https://doi.org/10.1016/j.celrep.2021.110210

CellPress

Cell Reports

CellPress
OPEN ACCESS

Article

Structural basis and mode of action for two broadly neutralizing antibodies against SARS-CoV-2 emerging variants of concern

Wenwei Li,[1,12] Yaozong Chen,[2,12] Jérémie Prévost,[3,4,12] Irfan Ullah,[5] Maolin Lu,[1,11] Shang Yu Gong,[3,6] Alexandra Tauzin,[3,4] Romain Gasser,[3,4] Dani Vézina,[3,4] Sai Priya Anand,[3,6] Guillaume Goyette,[3] Debashree Chaterjee,[3] Shilei Ding,[3] William D. Tolbert,[2] Michael W. Grunst,[1] Yuxia Bo,[7] Shijian Zhang,[8,9] Jonathan Richard,[3,4] Fei Zhou,[10] Rick K. Huang,[10] Lothar Esser,[10] Allison Zeher,[10] Marceline Côté,[7] Priti Kumar,[5] Joseph Sodroski,[8,9] Di Xia,[10] Pradeep D. Uchil,[1] Marzena Pazgier,[2,*] Andrés Finzi,[3,4,6,*] and Walther Mothes[1,13,*]

[1]Department of Microbial Pathogenesis, Yale University School of Medicine, New Haven, CT 06520, USA
[2]Infectious Disease Division, Department of Medicine, Uniformed Services University of the Health Sciences, Bethesda, MD 20814-4712, USA
[3]Centre de Recherche du CHUM (CRCHUM), Montreal, QC H2X 0A9, Canada
[4]Département de Microbiologie, Infectiologie et Immunologie, Université de Montréal, Montreal, QC H2X 0A9, Canada
[5]Department of Internal Medicine, Section of Infectious Diseases, Yale University School of Medicine, New Haven, CT 06520, USA
[6]Department of Microbiology and Immunology, McGill University, Montreal, QC H3A 2B4, Canada
[7]Department of Biochemistry, Microbiology and Immunology, and Center for Infection, Immunity, and Inflammation, University of Ottawa, Ottawa, ON K1H 8M5, Canada
[8]Department of Cancer Immunology and Virology, Dana-Farber Cancer Institute, Boston, MA 02115, USA
[9]Department of Microbiology, Harvard Medical School, Boston, MA 02115, USA
[10]Laboratory of Cell Biology, National Cancer Institute, National Institutes of Health, Bethesda, MD 20892, USA
[11]Present address: Department of Cellular and Molecular Biology, University of Texas Health Science Center at Tyler, Tyler, TX 75708, USA
[12]These authors contributed equally
[13]Lead contact
*Correspondence: marzena.pazgier@usuhs.edu (M.P.), andres.finzi@umontreal.ca (A.F.), walther.mothes@yale.edu (W.M.)
https://doi.org/10.1016/j.celrep.2021.110210

SUMMARY

Emerging variants of concern for the severe acute respiratory syndrome coronavirus 2 (SARS-CoV-2) can transmit more efficiently and partially evade protective immune responses, thus necessitating continued refinement of antibody therapies and immunogen design. Here, we elucidate the structural basis and mode of action for two potent SARS-CoV-2 spike (S)-neutralizing monoclonal antibodies, CV3-1 and CV3-25, which remain effective against emerging variants of concern *in vitro* and *in vivo*. CV3-1 binds to the (485-GFN-487) loop within the receptor-binding domain (RBD) in the "RBD-up" position and triggers potent shedding of the S1 subunit. In contrast, CV3-25 inhibits membrane fusion by binding to an epitope in the stem helix region of the S2 subunit that is highly conserved among β-coronaviruses. Thus, vaccine immunogen designs that incorporate the conserved regions in the RBD and stem helix region are candidates to elicit pan-coronavirus protective immune responses.

INTRODUCTION

Severe acute respiratory syndrome coronavirus 2 (SARS-CoV-2) is the third coronavirus to enter the human population since 2002 and is responsible for the coronavirus disease of 2019 (COVID-19) pandemic (Dong et al., 2020; Zhu et al., 2020). While over ~1 billion vaccines have been administered as of today (Baden et al., 2020; Folegatti et al., 2020; Logunov et al., 2021; Polack et al., 2020; Sadoff et al., 2021a, 2021b; Voysey et al., 2021), the pandemic remains uncontrolled in many countries and new variants, including the B.1.1.7 (SARS-CoV-2 α), B.1.351 (β), P.1 (γ), and B.1.617.2 (δ), are outcompeting previous variants due to higher transmissibility and elevated immune evasion (Campbell et al., 2021; Hoffmann et al., 2021; Planas et al., 2021a, 2021b; Prévost and Finzi, 2021; Volz et al., 2021). The spike glycoprotein (S) on the surface of the virus mediates entry into cells and is a prominent target for the host immune response including neutralizing antibodies. Consequently, S is a main immunogen for vaccine design. The Moderna, Pfizer-BioNTech, Johnson & Johnson, and AstraZeneca vaccines are all based on S immunogens (Baden et al., 2020; Folegatti et al., 2020; Polack et al., 2020; Sadoff et al., 2021a, 2021b; Voysey et al., 2021). S consists of a trimer of S1/S2 heterodimers. S1 contains the receptor-binding domain (RBD) that interacts with the cellular receptor angiotensin-converting enzyme 2 (ACE2) (Hoffmann et al., 2020; Li et al., 2003; Walls et al., 2020). S2 possesses

the fusion machinery, which can mediate host-viral membrane fusion after S1 shedding. Structural insights into the S glycoprotein have been gained by single particle cryo electron microscopy (SP cryoEM) of a soluble trimer comprising most of the ectodomain (Walls et al., 2020; Wrapp et al., 2020), as well as by cryo-electron tomography (cryoET) and SP cryoEM of native virus particles (Ke et al., 2020; Turoňová et al., 2020; Yao et al., 2020). These studies have revealed several distinct prefusion conformations, wherein three RBD adopt up or down orientations. Receptor ACE2 binds and stabilizes RBD in the up conformation (Lan et al., 2020; Shang et al., 2020; Xiao et al., 2021; Xu et al., 2021). Single-molecule fluorescence resonance energy transfer (smFRET) imaging of single S molecules on the surface of virus particles has provided real-time information for transitions between both RBD-up and -down conformations through one necessary intermediate (Lu et al., 2020).

Antibodies isolated from convalescent patients, vaccinated individuals, and previous work on the related SARS-CoV-1 and MERS-CoV viruses can be classified by their specificity for three main epitopes: the RBD, the N-terminal domain (NTD), and the S2 subunit (Barnes et al., 2020; Hastie et al., 2021; Jennewein et al., 2021; Ju et al., 2020; Liu et al., 2020; Montefiori and Acharya, 2021; Ullah et al., 2021). For each class, the conformational preferences for either RBD-up or RBD-down trimer configurations have been described. Antibodies directed against the RBD and NTD are often attenuated against emerging variants of concern due to escape mutations (Greaney et al., 2021a; Liu et al., 2021; McCallum et al., 2021; Starr et al., 2021; Weisblum et al., 2020). Although immune responses elicited by existing vaccines do offer protection to varying degrees against all known variants of concern (Skowronski et al., 2021; Tauzin et al., 2021), a booster shot to ensure sufficient protection from future emerging variants might be needed. Moreover, SARS-CoV-2 is the third β-coronavirus after SARS-CoV-1 and MERS-CoV to be transferred to humans in the 21st century, and given the large natural reservoir of similar viruses in species such as bats (Anthony et al., 2017; Ge et al., 2013; Letko et al., 2020; Menachery et al., 2015; Menachery et al., 2016; Wang et al., 2018), another pandemic caused by a new coronavirus is likely to happen again. These coronaviruses possess a conserved S2 domain, which raises the possibility of cross-reactive antibodies and cross-reactive vaccines. SARS-CoV-2 S is approximately 75% homologous to SARS-CoV-1 and 35% to MERS S (Grifoni et al., 2020; Zhou et al., 2020). Various cross-reactive antibodies have been identified (Hoffmann et al., 2020; Jennewein et al., 2021; Jette et al., 2021; Li et al., 2021b; Ma et al., 2020; Ng et al., 2020; Rappazzo et al., 2021; Song et al., 2021; Tian et al., 2020; Tortorici et al., 2021; Wang et al., 2020, 2021a; Wec Anna et al., 2020). Recently isolated antibodies capable of cross-neutralizing human coronaviruses bind to the conserved stem helix region on S2 (residues 1140–1165), reviving hopes for pan-coronavirus vaccines (Pinto et al., 2021; Sauer et al., 2021; Zhou et al., 2021).

We previously characterized two potent S-binding antibodies, CV3-1 and CV3-25, out of 198 antibodies isolated from convalescent patients (Jennewein et al., 2021; Ullah et al., 2021). CV3-1 targets the RBD of S1 and CV3-25 binds to the S2 ectodomain, the former displaying the most potent neutralizing activity among all antibodies (Abs) isolated. While CV3-1 is specific for the RBD of SARS-CoV-2, CV3-25 can recognize the S2 domains derived from several β-coronaviruses (Jennewein et al., 2021). Both antibodies protected against SARS-CoV-2 in animal models in prophylactic and therapeutic settings (Ullah et al., 2021). Here, we report the structural basis and mode of action for these two potent antibodies. We deployed cryoET of virus-like particles (VLPs) carrying the $S_{B.1.1.7}$ variant to determine the epitopes of these two antibodies. CV3-1 bound to the tip region (485-GFN-487 loop) within the receptor-binding motif (RBM), as confirmed by mutagenesis. Interestingly, we observed that most Ss in CV3-1-treated VLPs were triggered into the post-fusion conformation of S2 and caused S1 shedding into the supernatant. The data indicate that CV3-1 is a potent agonist and point to the 485-GFN-487 loop as an allosteric center critical for the activation of S1. In contrast, CV3-25 bound the stem helix in the connecting domain (CD) of S2 and blocked membrane fusion. Its binding was asymmetric, as S trimer was bound by 1 or 2 CV3-25 antigen-binding fragments (Fabs). Peptide competition narrowed the epitope and permitted the determination of the crystal structure of the S2 stem peptide bound to CV3-25 Fab. The structure revealed a unique bent conformation of the viral peptide with an upstream α-helical region followed by a random coil. Fitting of the X-ray structure into the cryoET density map demonstrated that an increasing degree of stem helix rotation was required to allow binding of one or both Fabs to avoid steric clashes. Compared with other recently reported S2-helix engaging antibodies (interacting with the helix N terminus, residues 1147–1157), CV3-25 interacts with the helix C terminus and the proximate hinge (residues 1153–1165). Given that the stem helix epitope is highly conserved among β-coronaviruses, immunogens featuring this S2 epitope are interesting candidates for vaccines to cover all variants and possibly exhibit pan-coronavirus efficacy. Moreover, since many antibodies that bind S are non-neutralizing, our work suggests that agonist features that prematurely trigger and thereby irreversibly inactivate S, or inhibition of membrane fusion, contribute to the ability of neutralizing antibodies to block SARS-CoV-2 infection.

RESULTS

CV3-1 and CV3-25 neutralize emerging SARS-CoV-2 variants

We first tested the ability of CV3-1 and CV3-25 to recognize and neutralize the emerging variants of concern, B.1.1.7 (SARS-CoV-2 α), B.1.351 (β), P.1 (γ), B.1.617.2 (δ) as well as variants of interest B.1.429 (ε), B.1.525 (η), B.1.526 (ι), and B.1.617.1 (κ). CV3-1 efficiently bound to cells expressing S glycoproteins from these different SARS-CoV-2 variants or carrying their individual mutations (Figures 1A and S1A). Despite the presence of variant-specific mutations in RBD, CV3-1 retained potent neutralizing activity (IC_{50} 0.004–0.014 μg/mL) (Figure 1B). Of note, CV3-1 binding to the B.1.1.7 variant with and without the additional E484K substitution was higher than binding to the S from the original Wuhan-Hu-1 strain (WT). CV3-25 was less potent with an IC_{50} in the range of ∼0.05–0.2 μg/mL, but remained effective against all variants in both binding ability and neutralization (Figures 1A, 1B, and S1B). Both CV3-1 IgG and the CV3-25 IgG GASDALIE mutant, which binds more strongly

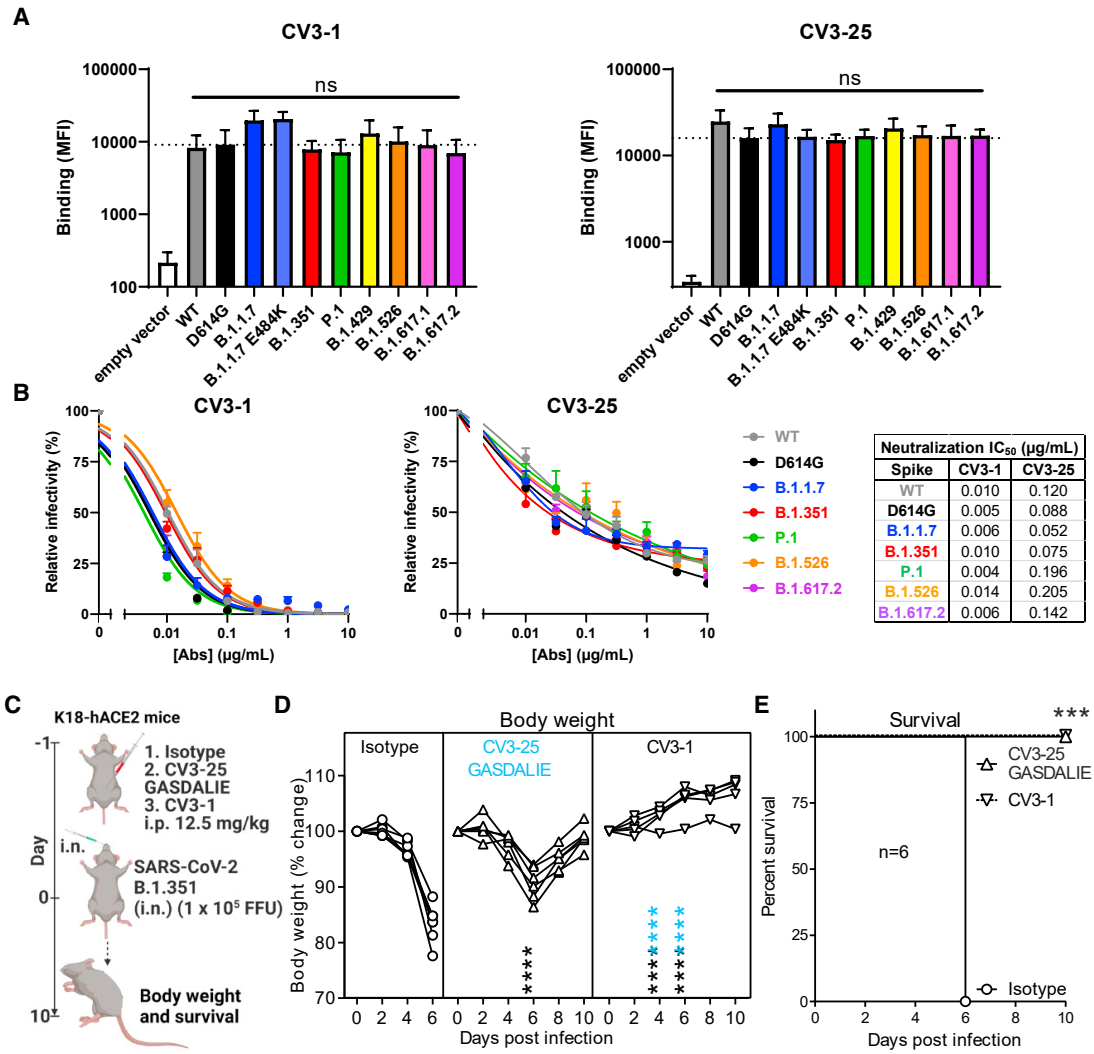

Figure 1. CV3-1 and CV3-25 neutralize emerging SARS-CoV-2 variants

(A) Cell-surface staining of 293T cells expressing full-length S from indicated variants by CV3-1 (left panel) and CV3-25 (right panel) monoclonal Abs (mAbs). The graphs show the median fluorescence intensities (MFIs). Dashed lines indicate the reference value obtained with S D614G. Error bars indicate means ± SEM. These results were obtained in at least 3 independent experiments. Statistical significance was tested using one-way ANOVA with a Holm-Sidak post-test (ns, non-significant).

(B) The ability of CV3-1 and CV3-25 mAbs to neutralize Wuhan-Hu-1 (WT), D614G mutant, (B)1.1.7, (B)1.351, P.1, (B)1.526, and (B)1.617.2 pseudoviruses infectivity in 293T-hACE2 cells was measured as indicated in Star Methods. IC_{50} values are shown. Error bars indicate means ± SEM. These results were obtained in at least 3 independent experiments.

(C) A scheme showing the experimental design for testing the *in vivo* efficacy of NAbs, CV3-1 WT and CV3-25 G236A/S239D/A330L/I332E (GASDALIE) mutant (12.5 mg IgG/kg body weight) delivered intraperitoneally (i.p.) 1 day before challenging K18-hACE2 mice with a lethal dose (1×10^5 FFU) of B.1.351 SARS-CoV-2. Human IgG1-treated (12.5 mg IgG/kg body weight) mice were used as control.

(D) Temporal changes in mouse body weight in experiment shown in (C), with initial body weight set to 100%.

(E) Kaplan-Meier survival curves of mice (n = 6 per group) statistically compared by log rank (Mantel-Cox) test for experiments as in (C). Grouped data in (D) were analyzed by two-way ANOVA followed by Tukey's multiple comparison tests. Statistical significance for group comparisons with isotype control are shown in black, and for those with CV3-25 GASDALIE are shown in blue. *, p <0.05; **, p <0.01; ***, p <0.001; ****, p <0.0001; mean values ± SD are depicted.

to Fcγ receptors, also protected *in vivo* against both the B.1.1.7 (α) (Ullah et al., 2021) and B.1.351 (β) variants of SARS-CoV-2 in the K18-hACE2 prophylactic mouse model (Figures 1C–1E). Both antibodies limited viral replication in the nose and lungs as well as its dissemination to the brain, thereby reducing the induction of pro-inflammatory cytokines (Figures S1C–S1F). These data demonstrate that in contrast to other antibodies that are attenuated against emerging variants (Greaney et al., 2021a; Liu et al., 2021; Starr et al., 2021; Weisblum et al., 2020), CV3-1 and CV3-25 remain potent against these variants and are therefore prime candidates to elucidate the mode of action and identify epitopes with pan-coronavirus activity.

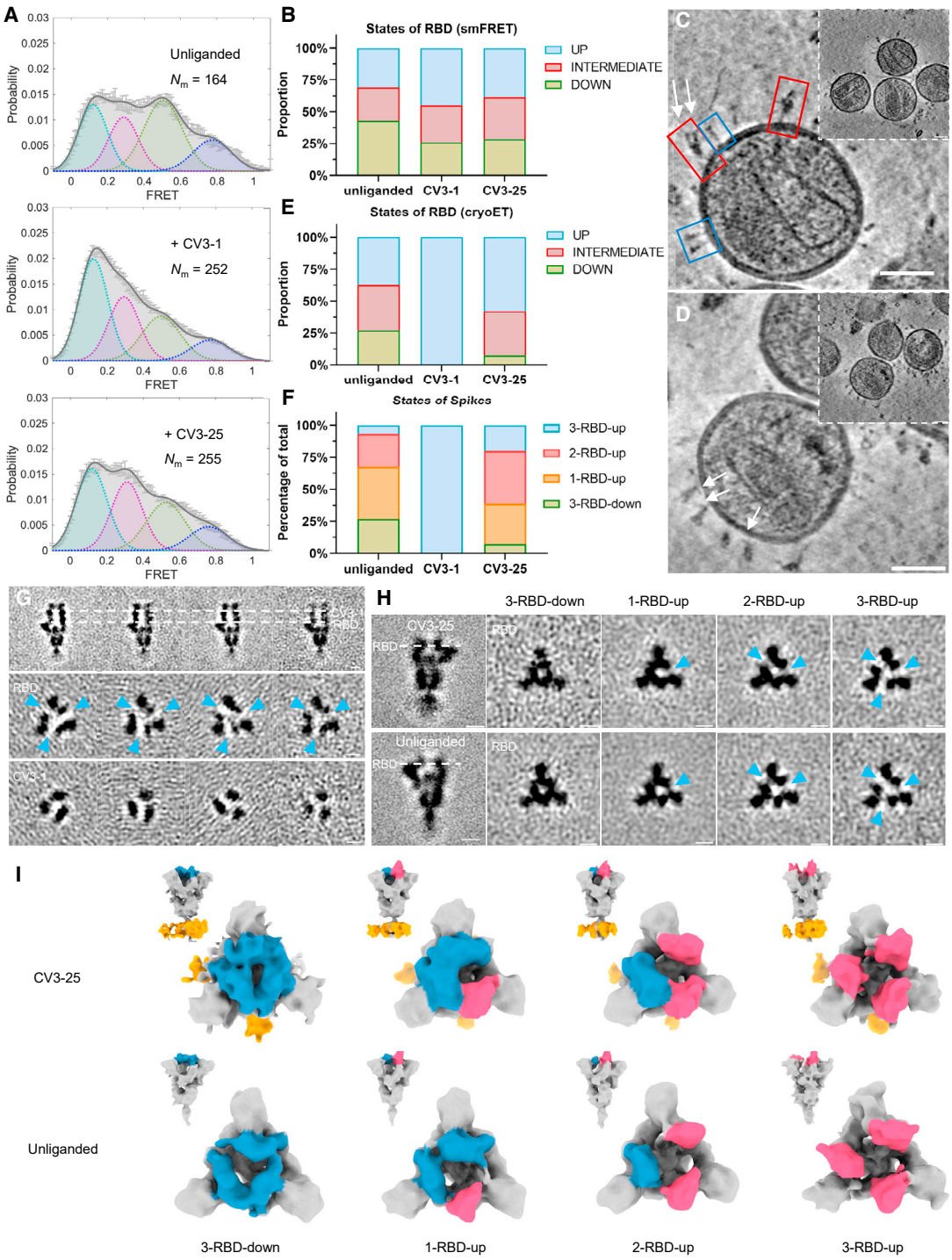

Figure 2. Conformational dynamics of $S_{B.1.1.7}$ bound with CV3-1 and CV3-25

(A) Conformational states of $S_{B.1.1.7}$ on lentiviral particles monitored by smFRET for unliganded, CV3-1- and CV3-25-bound $S_{B.1.1.7}$. FRET histograms with number (N_m) of individual dynamic molecules/traces compiled into a conformation-population FRET histogram (gray lines) and fitted into a 4-state Gaussian distribution (solid black) centered at 0.1 FRET (dashed cyan), 0.3 FRET (dashed red), 0.5 FRET (dashed green), and 0.8 FRET (dashed magenta).

(B) Proportion of different states of RBD identified by smFRET in (A). For parallel comparation with cryoET data, 0.8-FRET portion was omitted, due to its structural uncertainty.

(C and D) Zoomed-in views of SARS-CoV-2 pseudoviruses bearing S bound by CV3-1 (C) and CV3-25 (D) Fabs and representative slices of tomograms (insets). Scale bar, 50 nm. White arrows indicate bound Fabs. Red boxes, prefusion Ss. Blue boxes, post-fusion Ss.

(legend continued on next page)

S conformational preferences of CV3-1 and CV3-25 assessed by smFRET and CryoET

We utilized smFRET as a dynamic method and cryoET as a static method to characterize the conformational preferences of CV3-1 and CV3-25 for S of the B.1.1.7 variant ($S_{B.1.1.7}$). smFRET measures the conformational state within a single S1 protomer and indicated that the unliganded $S_{B.1.1.7}$ has access to four distinct conformational states, with the ~0.5 FRET state being the most occupied state (Figure 2A). We had previously established that these states correspond to the RBD-down (~0.5 FRET) and RBD-up (~0.1 FRET), a necessary structural intermediate (~0.3 FRET) in the transition from RBD-down to RBD-up that is likely observed in a protomer adjacent to an RBD-up, and a high-FRET state (~0.8) for which a structure is not available (Lu et al., 2020). CV3-1 redistributed the conformational landscape of S to the ~0.1 low-FRET state that corresponds to the RBD-up, thus mimicking receptor ACE2. CV3-25 redistributed the conformational landscape toward activation with an increase in the occupancy of the structural intermediate (~0.3 FRET) as well as the RBD-up state (~0.1 FRET) (Figures 2A and 2B). Overall, the conformational landscapes of the $S_{B.1.1.7}$ variant and the conformational preferences of CV3-1 and CV3-25 were similar to the original Wuhan-Hu-1 strain (Ullah et al., 2021).

We next used cryoET to identify the epitope for CV3-1 and CV3-25 and analyze their conformational preference by quantifying the proportion of antibody-bound trimers in the 3-RBD-down, 1-RBD-up, 2-RBD-up, and 3-RBD-up for $S_{B.1.1.7}$ on the surface of lentiviral particles. To improve incorporation of S into lentiviral particles for EM, the $S_{B.1.1.7}$ cytoplasmic tail was truncated (Figures 2C and 2D). The unliganded $S_{B.1.1.7}$ displayed a similar number of 3-RBD-down, 1-RBD-up, and 2-RBD-up conformations, with the 3-RBD-up conformation rarely observed (Figure 2F). CV3-1 clearly bound to the top of RBD with the RBD being oriented up (Figure 2C). Nearly all trimers with bound CV3-1 were in the RBD-up conformation (Figures 2E–2G). Binding to RBD is consistent with previous data that demonstrated the ability of CV3-1 to competitively inhibit ACE2-S binding *in vitro* (Jennewein et al., 2021).

In contrast, CV3-25 bound toward the bottom of S2 and all trimer configurations were observed (Figures 2D, 2F, 2H, and 2I). Compared with the unliganded S, CV3-25 binding redistributed the frequency of trimer configurations from the 3-RBD-down to the 1-, 2-, and 3-RBD-up configurations. To compare cryoET with smFRET data, we calculated the number of conformational states of individual RBD units, which is monitored by smFRET. This was done under the assumption that protomers neighboring to an RBD-up protomer are in an intermediate FRET state (Lu et al., 2020). Consequently, the 1- and 2-RBD-up not only feature 1 or 2 additional protomers in the RBD-up conformation, but also likely introduce a significant occupancy for structures exhibiting an intermediate FRET state (~0.3) (Figures 2E and 2F). While several caveats remain, such as the use of cytoplasmic tail-deleted S for EM (wt S for smFRET), the inability to see a structure corresponding to the intermediate FRET (~0.3), and as a consequence, not knowing if both, left, and right protomers neighboring an RBD-up, are in an intermediate FRET state, and the inability to assign a structure for the high-FRET state (~0.8), this is the first time that we can generate dynamic and static data for S on virus particles produced in the same cell type and assess them in parallel by smFRET and cryoET. Overall, there is qualitative agreement between cryoET and smFRET about how CV3-1 and CV3-25 alter the conformational landscape of S. Above-mentioned caveats make quantitative comparisons currently impossible. smFRET may detect more dynamic features, while cryoET may emphasize static features as previously discussed for the HIV-1 glycoprotein (Li et al., 2020).

CV3-1 binds to the 485-GFN-487 loop of RBD

To gain a higher resolution structure for CV3-1 bound to $S_{B.1.1.7}$, we imposed C3 symmetry on a subtomogram averaged structure and determined a ~12-Å map (Figures 3A and 3B, Figures S3A–S3C). The averaged cryoET structure showed three CV3-1 Fabs bound to the apex of the S trimer. Classification among these particles did not identify any subclass of Ss bound with only one or two CV3-1 Fabs (Figure 2D). Rigid-body fitting with a 3-RBD-down atomic model of $S_{B.1.1.7}$ (PDB: 7LWS [Gobeil et al., 2021]) left all three RBDs outside of cryoET density, while flexible fitting resulted in the conformational change from the RBD-down to the RBD-up state (Figure 3C and Video S1). We applied rigid fitting of the atomic structure of 1-up RBD (PDB: 7LWV [Gobeil et al., 2021]) to arrive at a model for CV3-1 Fab bound to $S_{B.1.1.7}$ (Figure 3D). Compared with the footprint of receptor ACE2 on RBD (PDB: 7KJ4 [Xiao et al., 2021]), CV3-1 preferentially bound to the extending loop that contains the $G^{485}F^{486}N^{487}$ residues (Figures 3D and 3E). We performed mutagenesis for the RBM and tested the abilities of CV3-1 and ACE2 to bind S mutants expressed on cells by flow cytometry. In agreement with the structural model, CV3-1 binding was preferentially affected by mutations in the 485-GFN-487 loop (Figures 3F and 3G). In contrast, ACE2 binding was sensitive to mutations within the RBM consistent with previous results (Greaney et al., 2021b; Starr et al., 2020). Importantly, all mutations within the 485-GFN-487 loop affecting CV3-1 binding also impaired ACE2 binding, indicating that escape mutations at these positions would likely result in a high fitness cost for the virus.

(E) Proportion of different states of RBD at different conditions from cyroET data. UP state was separated by focused classification on the RBD region. The remaining of the RBDs were defined as DOWN state if there was no up RBD on the same S; otherwise, they were considered as INTERMIEDATE state.
(F) Proportion of different RBD states of Ss on virions with and without Fabs bound. Ss were grouped into 3-RBD-down, 1-RBD-up, 2-RBD-up, and 3-RBD-up classes.
(G) Side views (top panel) and top views (middle and bottom panels) of subclasses of averaged S bound by CV3-1 Fabs.
(H) Side views (left column) of the consensus structure of unliganded (bottom) and CV3-25 bound (top) S and top views of subclass averages (right columns) obtained after focused classification on the RBD of S.In (G-H), dotted lines indicate the positions of top-view sections. Blue arrowheads point to the gap in density between RBD and the neighboring NTD that appears when the RBD moves into the UP-state. Scale bar, 5 nm.
(I) Segmentation of subclass averages of unliganded (bottom) and CV3-25 bound (top) S. Top views and side views (insets) are shown for 3-RBD-down, 1-RBD-up, 2-RBD-up, and 3-RBD-up classes. Down RBDs and up RBDs are shown in blue and red, respectively; CV3-25 Fabs are shown in orange.

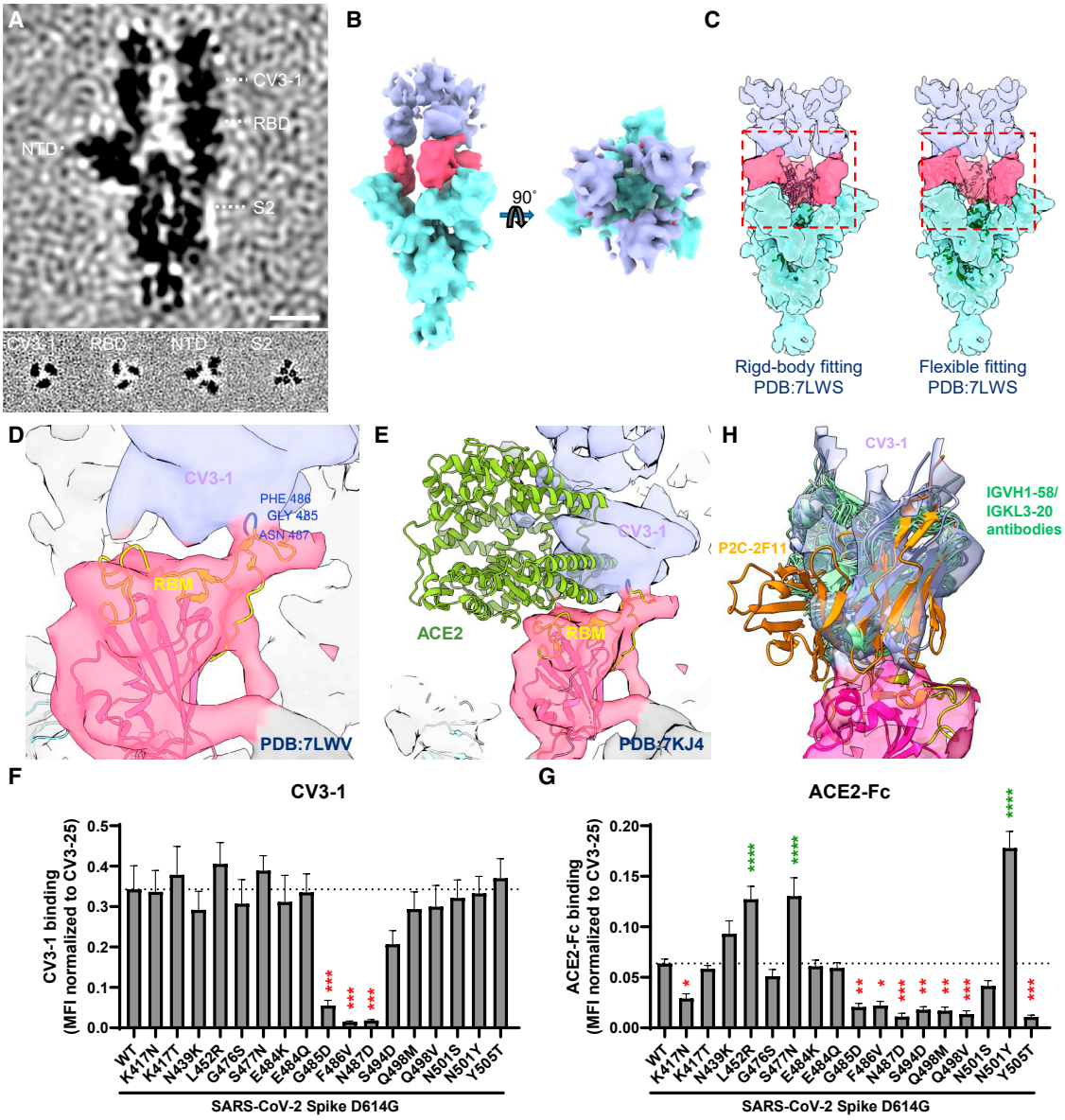

Figure 3. CV3-1 binds to the 485-GFN-487 loop of RBD

(A) Side view (top panel) and top views (bottom panel) of subtomogram average of CV3-1-bound S. Dotted lines indicate the positions of top-view sections. Scale bar, 5 nm.

(B) Segmentation of CV3-1 bound S. Side view (left) and top view (right) are shown. CV3-1 Fabs are shown in purple, RBDs are shown in red, and the rest of S in cyan.

(C) Fitting cryoET density map of CV3-1-bound S with 3-RBD-down atomic model of S (PDB: 7LWS). Top panel: rigid-body fitting. Bottom panel: flexible fitting.

(D and E) Zoomed-in view of cryoET map fitting with RBD-up atomic model (D, PDB: 7LWV) and ACE2-S atomic model (E, PDB: 7KJ4) at the interaction site.

(F and G) Binding of CV3-1 (F) and ACE2-Fc (G) to 293T cells expressing selected full-length S harboring RBM mutations. The graphs shown represent the MFIs normalized to the MFI obtained with CV3-25 staining of the corresponding mutant. Dashed lines indicate the reference value obtained with S D614G (WT). Error bars indicate means ± SEM. These results were obtained in at least 4 independent experiments. Statistical significance was tested using one-way ANOVA with a Holm-Sidak post-test (*p <0.05; **p <0.01; ***p <0.001; ****p <0.0001).

(H) RBD-based superimposition of CV3-1 and other ridge-binding antibodies. The SAbPred predicted CV3-1 model generated from rigid-body fitting to the CryoET map (semi-transparent surface) is colored in light purple and SAR-CoV-2 RBD in pink. The Fv regions of other ridge-binding Abs are shown as ribbons in indicated colors: IGHV1-58/IGKV3-20 antibodies in green and P2C-1F11 in orange.

A

	Virions	Prefusion Spikes
B.1.1.7	345	9967
B.1.1.7_CV3-1	298	1353
B.1.1.7_CV3-25	299	7739

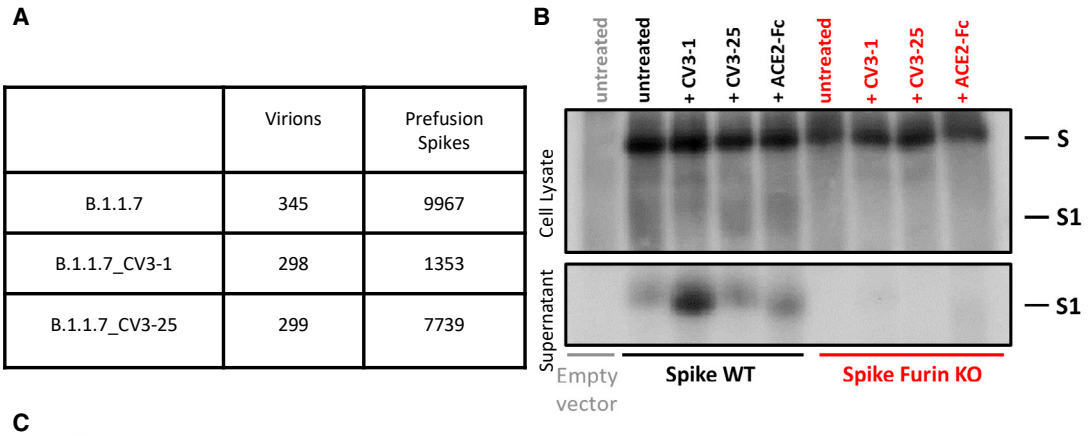

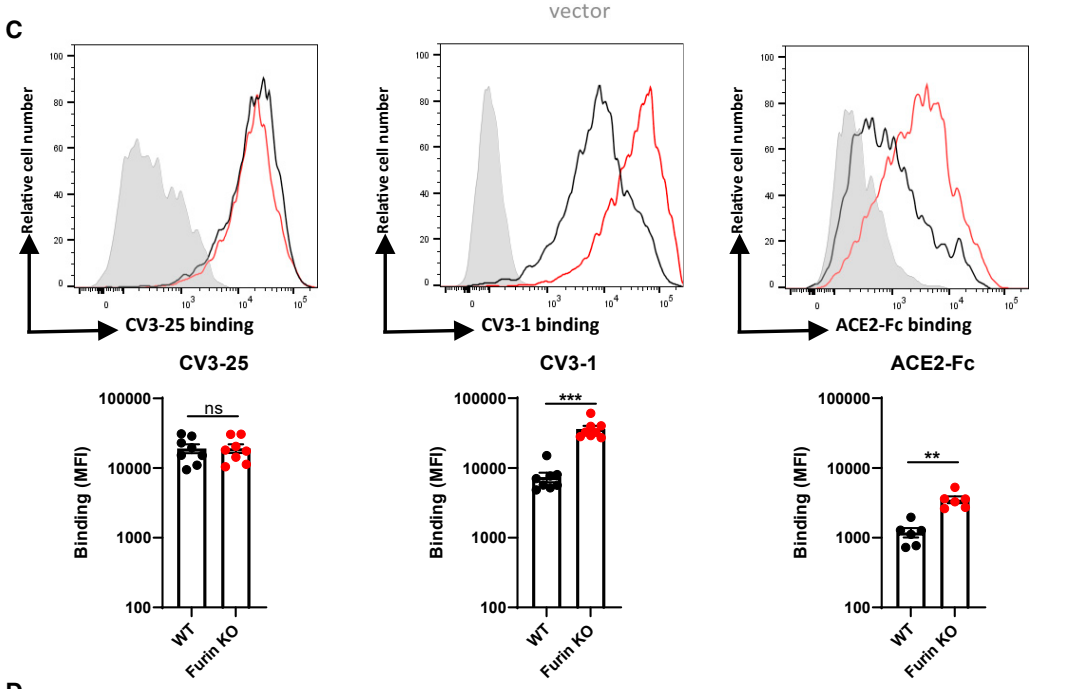

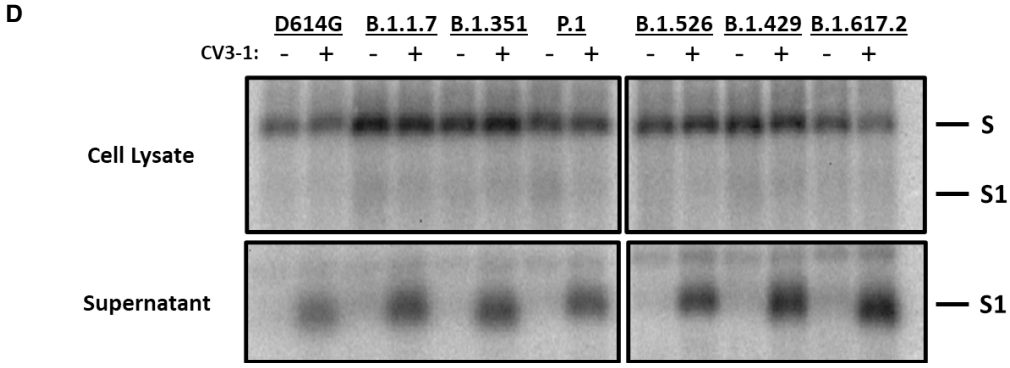

Figure 4. CV3-1 triggers S1 shedding

(A) Statistical table of pre-fusion S selected manually for cryoET analysis.

(B) S1 shedding was evaluated by transfection of 293T cells followed by radiolabeling in presence of CV3-1, CV3-25, or ACE2-Fc and immunoprecipitation of cell lysates and supernatant with CV3-25 and a rabbit antiserum raised against SARS-COV-2 RBD produced in-house. Furin KO = furin cleavage site knockout. These results are representative of two independent experiments.

(legend continued on next page)

CV3-1 uses IGHV1-58 heavy chain and IGKV3-20 light chain and has low level of somatic hypermutation (Jennewein et al., 2021). Recent studies have identified several neutralizing antibodies targeting the similar ridge region as CV3-1 (Dejnirattisai et al., 2021; Du et al., 2021; Li et al., 2021a; Robbiani et al., 2020; Tortorici et al., 2020; Wang et al., 2021b; Zost et al., 2020). Although produced from different convalescent patients, they share similar gene family usage in their heavy and light chains, IGHV1-58/IGKV3-20, and indicated potent neutralizing activities against SARS-CoV-2. These NAbs fit well into CV3-1 cryoET density map with almost same binding angles as CV3-1 (Figure 3H), suggesting this is a common class of NAbs that utilizes IGHV1-58/IGKV3-20 immunoglobulin genes and targets the RBD ridge region of SARS-CoV-2 S.

CV3-1 is a potent agonist triggering S1 shedding

SARS-CoV-2 S glycoproteins lacking the cytoplasmic tail are efficiently incorporated into lentiviral particles and form a dense array of Ss in the prefusion state (Dieterle et al., 2020; Ou et al., 2020; Schmidt et al., 2020; Yu et al., 2021). In contrast, the virus particles incubated with CV3-1 lost most prefusion Ss and displayed S in the post-fusion state (Figure 2C). Quantification of S numbers revealed that 83% of prefusion Ss, comparing with unliganded S, were lost after incubation with CV3-1 (Figure 4A). The structural characterization of CV3-1 bound to S shown above was performed with the remaining ~17% of prefusion Ss. Given the loss of S1 and activation of S2 into post-fusion conformation, we hypothesized that, besides competition with ACE2 (Jennewein et al., 2021), triggering S1 shedding likely contributed to SARS-CoV-2 neutralization efficacy of CV3-1. Radioactive labeling followed by immunoprecipitation of cell lysates and supernatant revealed that incubation with CV3-1 indeed released most S1 into the supernatant, with its activity well exceeding that of ACE2 (Figure 4B). S lacking the furin-cleavage site was resistant to CV3-1- and ACE2-mediated shedding. The loss of S1 following incubation of CV3-1 was also observed by flow cytometry on cells expressing S (Figure 4C). S lacking the furin-cleavage site was again resistant to shedding induced by CV3-1. In contrast to CV3-1, CV3-25 induced little or no shedding in all assays (Figures 4A–4D). Importantly, the ability of CV3-1 to neutralize the emerging variants B.1.1.7 (SARS-CoV-2 α), B.1.351 (β), P.1 (γ), B.1.526 (ι), B.1.429 (ε), and B.1.617.2 (δ) (Figure 1B) paralleled the ability of CV3-1 to shed S1 (Figure 4D). These data indicate that RBD-targeting antibodies can be potent agonists by prematurely activating S to impair virus entry, as previously observed for other RBM-directed antibodies (Ge et al., 2021; Walls et al., 2019; Wec Anna et al., 2020).

As previously shown using SP cryoEM, the S trimer displays significant tilt relatively to the viral membrane because of its highly flexible stalk region (Ke et al., 2020; Turoňová et al., 2020; Yao et al., 2020). Among the CV3-1-bound S that remained on the surface of virus particles, we sought to observe a change in the tilt angle of CV3-1-bound S. Quantification revealed a profound straightening of the S from an average tilt angle of ~57° for the unliganded S to only ~37° (Figures S2A–S2C). Apparently, the ACE2–mimicking activation of RBD by CV3-1 leads to long-range structural effects involving S2, likely weakening the S1-S2 interface and resulting in the shedding of S1. When evaluating antibody binding cooperativity, the Hill coefficient for CV3-1 binding was found to be highly positive ($h > 2$) (Figure S2D). Structurally, CV3-1 cannot bind the 3-RBD-down conformation due to a clash between heavy chain and adjacent RBD ridge. The highly positive cooperativity likely reflects a facilitated binding of CV3-1 to the second and third subunits in the RBD-up conformation. Our smFRET data have shown that SARS-CoV-2 S spontaneously transitions between RBD-down and RBD-up conformation. Thus, conformational capture of an RBD-up conformation by CV3-1 likely mediates the initial binding step.

CV3-25 binds the stem helix of S2

We employed a multipronged approach including cryoEM, cryoET, peptide competition, and X-ray crystallography to gain mechanistic insight into how CV3-25 achieves broad neutralization against emerging SARS-CoV-2 variants and other β-coronaviruses (Jennewein et al., 2021; Ullah et al., 2021). We first determined the cryo-EM structure of the SARS-CoV-2 S (HexaPro, prefusion-stabilized) (Hsieh et al., 2020) in the presence of CV3-25 Fab at an overall resolution of ~3.5 Å (Figures S4A–S4D). Map density analysis indicated the 1-RBD-up state was the dominant S conformation with a decreased local resolution in this region (Figure S4G). The density corresponding to the C-terminal stem region was less defined with a local resolution lower than 7 Å, but there was additional density for CV3-25 in the C-terminal stem region. 3D classification of the cryo-EM data barely improved the local density, suggesting incomplete Fab saturation for all available binding sites. Nevertheless, the data suggested that CV3-25 binds to the lower stem of the soluble HexaPro S.

Given that soluble S trimers are truncated, lack the transmembrane region, and feature a T4 foldon, we reasoned that cryoET of native S glycoproteins embedded into virus particles could provide more insight into CV3-25's epitope. We used cryoET followed by subtomogram averaging of ~7,000 prefusion Ss to examine CV3-25 binding to $S_{B.1.1.7}$. Subclassification revealed that about half of S had two CV3-25 Fabs bound to the stem of S2, and the other half had only one CV3-25 Fab bound (Figure S5). We further aligned the subtomograms with a mask for two CV3-25 Fabs to arrive at a ~10-Å resolution map. This structure places the CV3-25 epitope within the CD of the stem helix (Figures 5A, 5B, and 5F). Density for the second Fab was weaker, since ~ half of Ss had only one CV3-25 Fab bound.

As discussed above, classification of the S structures into 3-RBD-down, 1-, 2-, or 3-RBD-up revealed an overall shift toward activation for CV3-25-bound S (Figures 2E and 2F). Averaged

(C) CV3-25, CV3-1, and ACE2-Fc recognition of 293T cells expressing the full-length SARS-CoV-2 ancestral S with or without (furin KO) a functional furin cleavage site. Histograms depicting representative cell-surface staining of cells transfected with wild-type S (black line), furin KO (red line), or with an empty vector (light gray). Error bars indicate means ± SEM. These results were obtained in at least 6 independent experiments. Statistical significance was tested using a Mann-Whitney U test (**p <0.01; ***p <0.001; ns, non-significant).
(D) CV3-1 induced S1 shedding of S from selected emerging variants, measured as in (B).

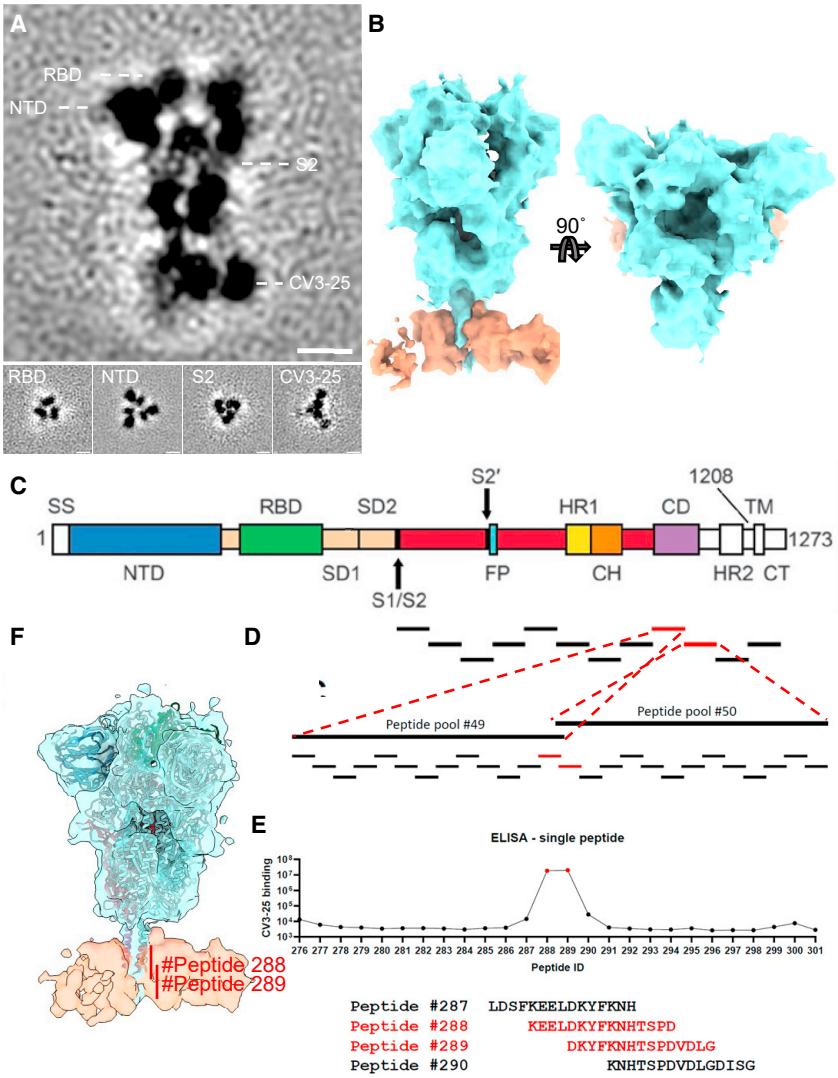

Figure 5. CV3-25 binds to a conserved epitope in S2

(A) Side view (top panel) and top views (bottom panel) of subtomogram averaged CV3-25-bound S. Dotted lines indicate the positions of top-view sections. Scale bar, 5 nm.

(B) Segmentation of CV3-25-bound S. Side view (left) and top view (right) are shown. CV3-25 Fabs are shown in orange, and S is shown in cyan.

(C) SARS-CoV-2 S sequence depicting the different subunits and domains composing the full-length S protein. With permission from AAAS (Wrapp et al., 2020).

(D) Pools of peptide covering the whole S2 subunit sequence were used to identify the linear region recognized by CV3-25 mAb. Indirect ELISA was performed using SARS-CoV-2 S2 peptide pools and incubation with the CV3-25 mAb. Peptide pools covering the connector domain (CD) region with significant positive signal were highlighted in red (peptide pools #49 and #50). Depiction of the SARS-CoV-2 S individual peptides from the peptide pools #49 and #50, with a 4-amino-acid residue overhang. Individual peptides covering the S2 CD region were used to identify the region recognized by CV3-25 mAb.

(E) Indirect ELISA was performed using SARS-CoV-2 S2 individual peptides (from peptide pools #49 and #50) and incubation with the CV3-25 mAb. CV3-25 binding was detected using HRP-conjugated anti-human IgG and was quantified by relative light units (RLUs). Single peptides with significant positive signal were highlighted in red (peptides #288 and #289). Amino acid sequence of peptides recognized by CV3-25 (peptides #288 and #289, shown in red) and of neighboring peptides not recognized by CV3-25 (peptides #287 and #290, shown in black).

(F) Rigid fitting cryoET density map of CV3-25-bound S with atomic model of closed prefusion S (PDB:6XR8). Peptides #288 and #289 location at the CV3-25 binding site are indicated in red.

structures focusing on RBD showed three bound CV3-25 Fabs in 1-RBD-up and 2-RBD-up Ss, while only two CV3-25 Fabs bound to 3-RBD-down and 3-RBD-up average structures (Figure S2E). These structures confirmed that CV3-25 binds to all prefusion S configurations, consistent with previous biochemical results as well as smFRET (Lu et al., 2020). Any observed asymmetry was not due to the tilt of the S, as the average tilt barely changed upon binding of CV3-25 (Figures S2A–S2C), consistent with a neutral antibody binding cooperativity (Hill coefficient ≈ 1) (Figure S2D).

Peptide screening maps CV3-25 epitope to the S residues 1149–1167

To gain atomic insight, we screened S2 peptides for binding to CV3-25 with the goal of isolating peptides suitable for X-ray crystallography. The first insight that CV3-25 binds a linear peptide was gained from Western blotting following SDS-PAGE. CV3-25 was clearly able to bind to S2 as well as the S2-containing S precursor under fully denaturing conditions and independently of N-linked glycans (Figures S6A and S6B). We then tested a set of peptides (15-mer) spanning the entire S2 subunit including the CD and performed two rounds of ELISA to identify peptides capable of binding CV3-25 (Figures 5C–5E). The identified peptides (#288 and #289) were also tested in competition assays, and the binding was quantified using surface plasmon resonance (SPR) assays (Figures S6C and S6D). Peptide #289 was the most potent in all assays with a K_D of 29 nM and efficiently blocked CV3-25 neutralization (Figures S6E and S6F). Peptides #288 and #289 mapped to the S2 stem helix region (Figure 5F), consistent with the CV3-25 binding region indicated in the cryoET averaged structure.

CV3-25 binds to a conserved S2 peptide in a bent conformation

To obtain molecular insight into CV3-25 interaction with the S2 stem peptide, we determined the co-crystal structure of

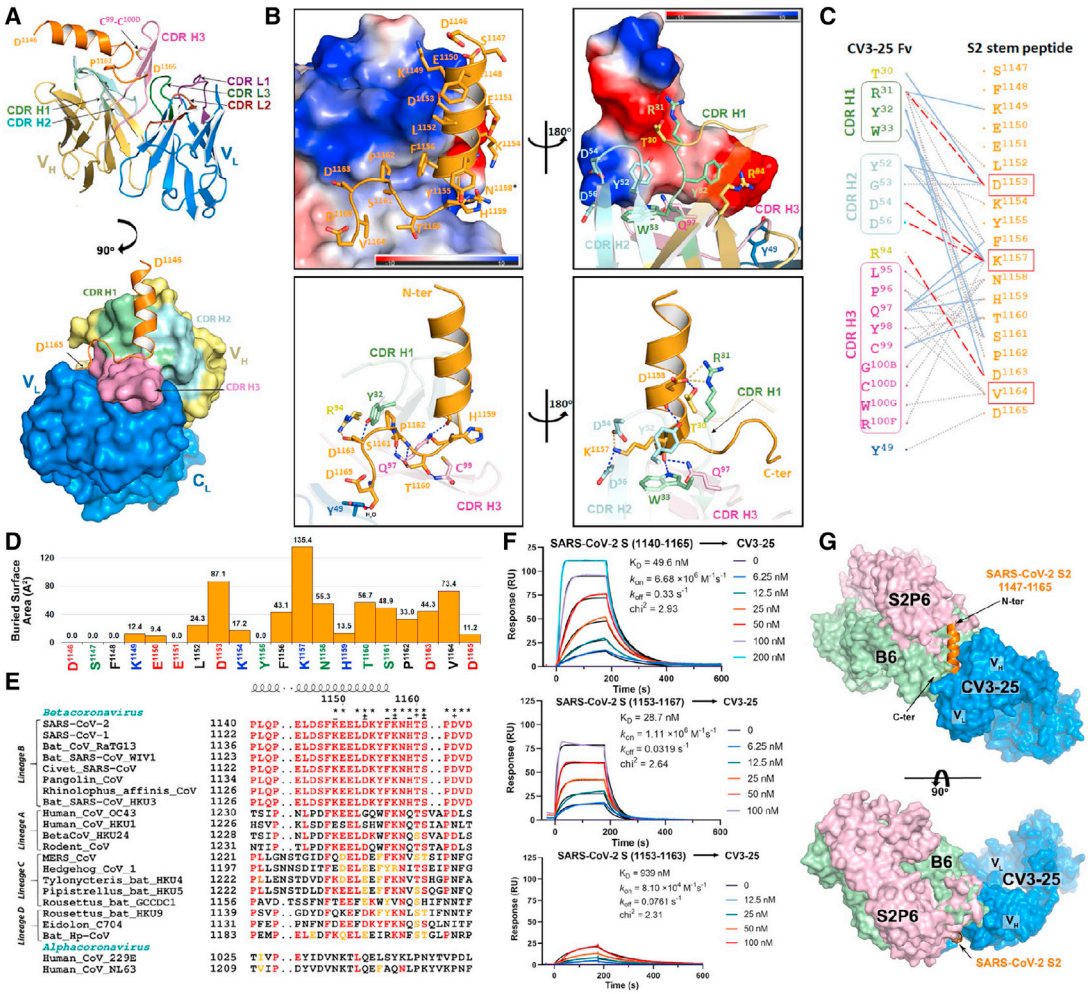

Figure 6. Molecular details of interaction of CV3-25 with SARS-CoV-2 stem peptide spanning residues 1140–1165 of S2

(A) Crystal structure of CV3-25 Fab in complex with $S2^{1140-1165}$ stem peptide (orange) in two orthogonal views. S2 peptide (orange) assumes a bent conformation with the N-terminal α-helical portion binding primarily to CDRs H1 and H2 (light green and cyan, respectively) and the random coil region interacting with CDR H3 (light pink). A non-canonical disulfide (C^{99}-C^{100D}) stabilizes the protruding CDR H3 and likely strengthens its interactions with the S2 C-terminus.

(B) Close-up views into the CV3-25 Fab-$S2_{1140-1165}$ peptide interface. In the top panel, the electrostatic potential is displayed over the molecular surface of CV3-25 (left) or S2 peptide (right) with 180° views of the complex with the putative glycosylation site N1158 marked with a black asterisk. The bottom panel shows the network of H-bonds and salt bridges formed at the interface with orientations of complex as in the top panel. Salt bridges and hydrogen bonds (<3.5 Å) are denoted as yellow and blue dashed lines, respectively. A total of 11 H-bonds and 4 salt bridges are formed at the interface, with D^{1153} and K^{1157} of the S2 peptide contributing the majority of the hydrophilic contacts. The S2 bend and loop conformation (1158–1165) are stabilized by heavy-chain CDR contacts. In addition, π-proline-π sandwich (F^{1156}- P^{1162}-Y^{32}) stacking formed between the conserved S2 and CDR H1 further stabilizes the interface. CV3-25 light chain contacts are limited to only a single water-mediated H-bond to the C-terminal D^{1165} of S2.

(C) The network of interaction (5-Å cutoff) between CV3-25 and S2 interface. Salt bridges and H-bonds (bond length less than 3.5 Å) are shown as red dashed and blue solid lines, respectively. Hydrophobic interactions or bond distances between 3.5 and 5.0 Å are shown as gray dotted lines.

(D) Diagram showing the buried surface area (BSA) of each individual S2 peptide residue in the CV3-25 Fab-S2 peptide complex. The BSA values of individual S2 residues were calculated using PISA[15] and are shown as the average of the values obtained for two complexes in the asymmetric unit of the crystal.

(E) Sequence alignment of the S glycoprotein stem-peptide regions from representative beta-coronaviruses and two human alpha-coronaviruses. The Fab-peptide interface residues are marked with (*) and those involved in hydrogen bonds or salt bridges by side chain, main chain, or both are marked with (+), (−), and (±), respectively. The identical residues as compared with SARS-CoV-2 are colored in red with conservative changes marked in orange and non-conservative changes in black.

(F) SPR sensor grams of three SARS-CoV-2 S2 peptides binding to the immobilized CV3-25 IgG on a Protein A chip. The experimental data (colored) are fitted to a 1:1 Langmuir model (black), and the resulting kinetic constants are as shown. The minimal peptide recognized by CV3-25 with a low K_D value (~1 μM) is 1153–1163. A 2- or 4-residue C-terminal extension leads to a 18- to 32-fold increase in the binding affinity.

(G) S2-peptide-based structural superimposition of CV3-25 (blue) and two other S2-binding antibodies, S2P6 (PDB: 7RNJ, pink), and B6 (PDB: 7M53, pale green) in two orthogonal views. SARS-CoV-2 S2 peptide (1147–1165) bound to CV3-25 is shown as orange ribbon.

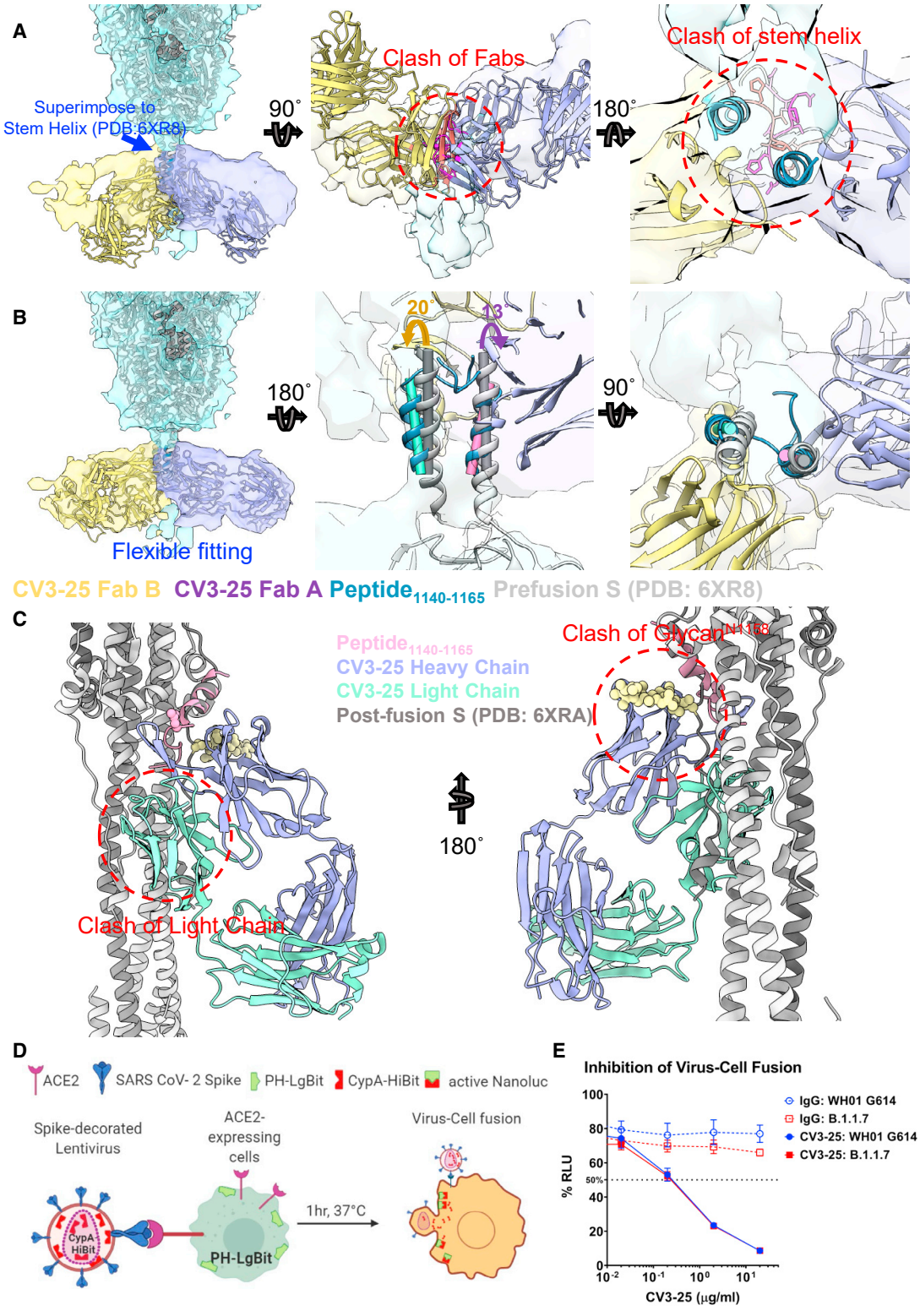

Figure 7. CV3-25 inhibits S-mediated virus fusion

(A) The crystal structures of the CV3-25 Fabs (purple and yellow) with the $S2_{1140-1165}$ peptides (blue) were superimposed onto the stem helix of the prefusion S atomic model (gray, PDB 6XR8) and fitted into the CV3-25 CryoET structure. Left panel: side view indicates that CV3-25 does not dock into the cryoET density map. There are clashes between two Fabs (middle panel, bottom view) and the tails of binding stem helix (right panel, top view).

(legend continued on next page)

CV3-25 Fab with a synthetic peptide spanning residues 1140–1165 (26mer) of SARS-CoV-2 S. The structure was solved to 2.1-Å resolution and allowed us to resolve 20 of the 26 residues in relation to the Fab paratope (Figures 6, S7, and Table S2). When bound to CV3-25 Fab, the peptide adopted a bent conformation with the N-terminal half of the peptide (residues 1146-DSFKEELDKYFK-1157), forming an α-helix and the C-terminal half of a random coil (residues 1158-NHTSPDVD-1165) with a bend of ~95° between the two (Figure 6A). This bent conformation fit well with the long complementary determining region (CDR) H3 loop of the Fab (16 residues long) that is stabilized by extensive H-bonds, salt bridges, and intra-molecular π-π stacking between residues Y^{1155} and H^{1159} of the peptide (Figures 6B–6D and S7). A rare CDR H3 disulfide bond between residues C^{99} and C^{100D} also stabilizes the CDR H3 hairpin that tightly associates with the S2 peptide random coil. Interestingly, the S2 stem region recognized by CV3-25 is conserved among the B lineage of β-coronaviruses (Figure 6F), with several key epitope residues also conserved among A, C, and D lineages. Indeed, CV3-25 is able to recognize the stem helix peptide derived from MERS S (Hurlburt et al., 2021). This suggests that CV3-25 displays cross-reactivity with coronaviruses beyond the B-lineage (Jennewein et al., 2021; Ullah et al., 2021). Furthermore, although crystallographic analyses confirm that residues 1149 to 1165 of the S2 stem to interact with CV3-25 (Figure 6D), SPR analyses using S2 peptide truncations indicate that CV3-25 may also interact with residues following D^{1165}, the terminal S2 residue used in crystallographic studies. These contacts could be mediated by the light chain of CV3-25 that is positioned to accommodate the C-terminal extension of the peptide (Figure 6A). Additionally, a potential N-linked glycosylation site (PNGS) is present in the CV3-25 epitope (N1158), but the residue is positioned in a way that the glycan protrudes on the opposite side of the stem helix. Removal of the N1158 PNGS using different substitution did not affect CV3-25 binding, which is in line with its glycan independence (Figures S6B, S6F, and S6G). Of note, the S2 recognition site and angle of approach of CV3-25 differentiate it from B6, an anti-MERS-CoV cross-reactive S2-binding Nab, as well as two known human NAbs specific for SARS-CoV-2 stem helix, CC40.8 and S2P6 (Pinto et al., 2021; Sauer et al., 2021; Zhou et al., 2021) (Figure 6G, PDB of CC40.8 not available to date). B6, CC40.8, and S2P6 mainly interact with the N-terminal stem α-helix and barely contact with the C-terminal loop, as recognized and reconfigured by CV3-25. Additionally, the antibody class defined by B6, CC40.8, and S2P6 have been shown to bind to the hydrophobic face of the stem helix, while CV3-25 binds to an adjacent face of the stem helix, which involves the important interaction with several charged residues (notably D1153 and K1157) as depicted in Figure 6. Mutations of these key residues completely abrogated CV3-25 binding (Figures S6F and S6G). This unique binding mode of CV3-25 indicates it as the first representative of a new class of anti-S2 antibodies with broad reactivity against β-coronaviruses.

To conceptualize the X-ray structure of the peptide bound to CV3-25 in the context of the S trimer, we superimposed two CV3-25 Fabs structures to the stem helix of the S trimer (PDB: 6XR8 [Cai et al., 2020] (Figure 7A). Direct superposition results in a clash of the Fabs and a mismatch of the Fab with the density map observed in the cryoET structure (Figure 7A). The random coil of the stem helix bound with CV3-25 points toward the center of the stem helix bundle producing a clash when two coils occupy the center region (Figure 7A). By performing flexible fitting, we arrived at a structure for two CV3-25 Fabs bound to the S trimer, in which the helix and flexible turn are almost maintained at the original position for the first Fab (rotated by about 13°), and are shifted outward and rotated by about 20° for the second Fab (Figure 7B and Video S2). The increasing need for dislocation and rotation likely explains that binding additional Fabs comes at an energy cost resulting in an asymmetric arrangement of one or two CV3-25 Fabs bound to S.

Superimposition of the CV3-25/peptide structure to post-fusion S (PDB: 6XRA) (Cai et al., 2020) indicates that the light chain of CV3-25 would clash with HR1 of the adjacent protomer (Figure 7C). Furthermore, in post-fusion conformation, the stem helix unwinds a full turn, resulting in a clash between the glycan at ASN1158 and the heavy chain of CV3-25 (Figure 7C). These observations suggest that the structure of CV3-25 bound to S is incompatible with the post-fusion conformation of S. Indeed, we observed potent inhibition of membrane fusion by CV3-25 in a virus-to-cell fusion assay that uses nano-luciferase complementation (Figures 7D and 7E). As observed for CV3-1, CV3-25 also exhibits potent inhibitor function.

DISCUSSION

Here, we describe the structures and mode of action of two potent anti-SARS-CoV-2 S antibodies. Both antibodies remained effective against emerging variants of concern and therefore were prime candidates to elucidate mode of action and identify epitopes with pan-coronavirus activity. CV3-1 stabilized the RBD in the "RBD-up" conformation and triggered potent shedding of S1. The ability of CV3-1 to neutralize variants of concern correlated with its ability to shed S1 and inactivate S. In contrast, CV3-25 bound to a highly conserved epitope in the stem helix in the S2 subunit and inhibited membrane fusion.

(B) Flexible fitting with a combined model containing the CV3-25_$S2_{1140-1165}$ crystal structure and prefusion S structure (gray, 6XR8) onto the cryoET structure. CV3-25 Fabs (purple and yellow) dock into the cryoET density map (left panel). The torsions of binding stem helix (blue, helix axes in cyan and pink, respectively) after fitting, comparing with original position of stem helix in 6XR8 (gray, helix axes in dark gray), were shown in middle and right panels. The third protomer was omitted for clarity.

(C) Superimposition of peptide-bound CV3-25 (purple, heavy chain; green, light chain) to the fusion S (gray, PDB 6XRA). The peptide (pink) was aligned to the stem helix in the S. The glycan on residue ASN1158 is shown in sphere representation (yellow). Possible clashes are indicated in red circles.

(D and E) Investigation of virus-cell fusion activity in presence and absence of CV-35 mAb by the split nanoluc complementation assay. A scheme of the spilt nanoluc complementation assay experimental design was shown in (C). Error bars indicate means ± SEM.

We believe that both epitopes of these two antibodies are of interest for passive and active immunization strategies against emerging variants.

The cryoET structure of CV3-1 to S suggested binding to the 485-GFN-487 loop of RBD, an interpretation confirmed by mutagenesis. While mutations in these positions abrogate the binding of CV3-1 to S, they are rarely observed among circulating strains, suggesting that they are associated with a high fitness cost likely due to their importance in ACE2 interaction, in agreement with previous studies on the role of SARS-CoV-2 S mutations on ACE2 binding (Chen et al., 2021; Starr et al., 2020). Interestingly, CV3-1 exhibited potent agonist features indicating that it hits an allosteric site that is critical for the ability of ACE2 to induce conformational changes that lead to fusion. Consistent with this observation, CV3-1 induced potent shedding and the straightening of Ss indicative of allosteric signaling from the RBD all the way to the S2 stem region. This allosteric signaling likely weakens the S1-S2 interface leading to the observed shedding of S1. While CV3-1 is specific against SARS-CoV-2, it remained active against all tested variants of concern and variants of interest and protected K18-hACE2 transgenic mice from lethal challenges using the B.1.351 variant of concern. The potent agonist features within the ACE2 binding site may also open an opportunity for small-molecule inhibitors that prematurely activate S not unlike CD4 mimetics in the case of HIV-1 envelope (Laumaea et al., 2020).

CV3-1 belongs to a class of RBD-specific antibodies that use IGHV1-58 and IGKV3-20 immunoglobulin variable precursor genes, approaching the RBD ridge region with a certain angle (Dejnirattisai et al., 2021; Du et al., 2021; Li et al., 2021a; Robbiani et al., 2020; Tortorici et al., 2020; Wang et al., 2021b; Zost et al., 2020) (Figure 3H). Whether these IGHV1-58/IGKV3-20 Nabs similarly trigger S1 shedding requires further investigation. Interestingly, P2C-1F11 had been reported as a potent inducer for S1-shedding by binding at the tip region of RBD (Ge et al., 2021). When P2C-1F11 was superimposed with the cryoET-map-fitted CV3-1 based on the bound RBD, it revealed that P2C-1F11 interacts with both the ridge and the RBM from a different orientation (Figure 3H), indicating that the molecular mechanism of shedding requires further studies. Clearly, antibodies that target the tip region of RBD do not always shed, and shedding can be triggered by binding to other regions of RBD (Ge et al., 2021; Long et al., 2021; Wec Anna et al., 2020). A full understanding of how RBD-targeting antibodies trigger S1 activation and shedding likely requires a molecular understanding how S1 evolved to be activated by receptor.

The structures of CV3-25 with an S peptide and intact S on the surface of virus particles revealed that it binds to the S2 stem in a region conserved among β-coronaviruses. At the time of our manuscript preparation, the structure of the CV3-25-S2 peptide (residues 1149–1167) complex was solved by Hurlburt et al. (2021), at similar resolution. The structures are virtually the same, with identical conformation of the S2 peptide bound to CV3-25. Unlike other recently reported anti-S2 antibodies, CC40.8 and S2P6, which mainly recognize the stem helix (residues 1147–1157) and barely interact with the hinge region (Pinto et al., 2021; Zhou et al., 2021), CV3-25 also engages the hinge peptide known to be responsible for the tilting of Ss with respect to the membrane (residues 1153–1165) (Ke et al., 2020; Turoňová et al., 2020). The highly conserved Pro1162 in the hinge region could be responsible to disrupt helical secondary structures and to form flexible structures. This added ability of CV3-25 likely offers an advantage in capturing an easily accessible epitope in the hinge region and subsequently progressively twisting the helix to establish contact with the α-helical region of the stem. The relative conservation of this hinge is likely related to the observed allosteric communication from the RBD all the way down to S2. The post-fusion conformation of S forms a six-helix bundle structure when pulling two membranes together for fusion. This conformational change probably involves unwinding of the stem helix and loop to helix transition for the loose loop at the lower end. CV3-25 binding at both helix region and the random coil at the stem helix likely interrupts this S2 refolding, thus inhibiting membrane fusion.

One of the most exciting aspects of CV3-25 is its linear peptide epitope, which offers easy access to exploration of its potential as an immunogen. As the structure of the native S on the surface of virus particles revealed, access of CV3-25 is hindered by the need for rotation of the stem helix. However, such conformational readjustment is not needed for an immunogen. As such, eliciting antibodies targeting this S2 stem epitope using peptide or scaffold-presented peptide immunogens is predicted to be easier than when the entire S trimer is the antigen. The potential of the CV3-25 epitope described herein should be explored as a candidate immunogen for vaccines that could be effective against all emerging variants and possibly exhibit pan-coronavirus efficacy.

Limitations of the study

Our study suggests that neutralizing antibodies of SARS-CoV-2 are also inhibitors of virus entry, e.g., by causing shedding of S1 or inhibiting membrane fusion, a hypothesis that requires future studies. We observed that potent neutralization of SARS-CoV-2 emerging variants of concern by CV3-1 correlated with shedding of S1. A detailed understanding of how CV3-1 activates and sheds S1 requires higher resolution structures, and comparative studies among RBD-targeting antibodies are needed to understand what antibodies trigger S1 shedding.

We arrived at a model for CV3-25 bound to the S2 stem helix of S by flexible fitting of the X-ray structure of peptide bound to CV3-25 and 6XR8 into our cryoET density map. Structure validation of this model requires solving high-resolution structure of the native S glycoprotein bound to CV3-25. The evaluation of the CV3-25 epitope within the S2 stem as an immunogen with pan-coronavirus potential requires experimental vaccination studies.

DISCLAIMER

The views expressed in this presentation are those of the authors and do not reflect the official policy or position of the Uniformed Services University, U.S. Army, the Department of Defense, or the U.S. Government.

STAR★METHODS

Detailed methods are provided in the online version of this paper and include the following:

- KEY RESOURCES TABLE
- RESOURCE AVAILABILITY
  - Lead contact
  - Materials availability
  - Data and code availability
- EXPERIMENTAL MODEL AND SUBJECT DETAILS
  - Cell lines
  - Antibodies
  - Mice
- METHOD DETAILS
  - Plasmids and site-directed mutagenesis
  - Cryo-electron tomography sample preparation
  - Cryo-electron tomography data collection
  - Cryo-electron tomography data analysis
  - SARS-CoV-2 infection and treatment conditions
  - Focus forming assay
  - Measurement of viral burden
  - Analyses of signature inflammatory cytokines mRNA
  - Virus-cell fusion inhibition assay
  - smFRET imaging of S on SARS-CoV-2 VLPs
  - Recombinant protein expression and purification
  - Surface plasmon resonance
  - Cryo-EM sample preparation and data collection
  - CryoEM data processing, model building and analysis
  - Crystallization and structure determination of CV3-25 with S2 stem peptide
  - Flow cytometry analysis of cell-surface staining
  - Viral neutralization assay
  - Radioactive labeling and immunoprecipitation
  - Peptide scanning ELISA
  - Western blotting
- QUANTIFICATION AND STATISTICAL ANALYSIS
  - Schematics

SUPPLEMENTAL INFORMATION

Supplemental information can be found online at https://doi.org/10.1016/j.celrep.2021.110210.

ACKNOWLEDGMENT

We thank Dr. Shenping Wu at Yale CryoEM facility for her technical assistance and Dr. Zhuan Qin at University of Oxford for discussion on image processing. The authors thank the CRCHUM Animal Facility, BSL3, and Flow Cytometry Platforms for their technical assistance. We thank Dr. Stefan Pöhlmann and Dr. Markus Hoffmann (Georg-August University) for the plasmids coding for SARS-CoV-2 and Daniel Kaufmann for the S2 15-mer peptide panel. The authors are grateful to MediMabs for providing their rabbit immunization protocol used to generate the anti-SARS-CoV-2 RBD polyclonal antibody. CV3-1 and CV3-25 antibodies were produced using the pTT vector kindly provided by the Canada Research Council. Crystallographic data were collected at the Stanford Synchrotron Radiation Light Source, SLAC National Accelerator Laboratory, which is supported by the U.S. Department of Energy (DOE), Office of Science, Office of Basic Energy Sciences, under contract number DE-AC02-76SF00515. The SSRL Structural Molecular Biology Program is supported by the DOE Office of Biological and Environmental Research and by the National Institutes of Health (NIH), National Institute of General Medical Sciences. This work was supported by a Canadian Institutes of Health Research (CIHR) operating grant Pandemic and Health Emergencies Research/Project #465175 to M.P., W.M., and A.F., an NIH R01 AI163395-01 to W.M., by le Ministère de l'Économie et de l'Innovation (MEI) du Québec, Programme de soutien aux organismes de recherche et d'innovation to A.F., the Fondation du CHUM, a CIHR foundation grant #352417 to A.F., CIHR stream 1 and 2 for SARS-CoV-2 Variant Research to A.F. and M.C., an Exceptional Fund COVID-19 from the Canada Foundation for Innovation (CFI) #41027 to A.F., the Sentinelle COVID Quebec network led by the Laboratoire de Santé Publique du Quebec (LSPQ) in collaboration with Fonds de Recherche du Québec-Santé (FRQS) and Genome Canada—Génome Québec, and by the Ministère de la Santé et des Services Sociaux (MSSS) and MEI to A.F. A.F. and M.C. are recipients of Canada Research Chairs on Retroviral Entry no. RCHS0235 950232424 and CRC in Molecular Virology and Antiviral Therapeutics, respectively. J.P. and S.P.A. are supported by CIHR doctoral fellowships, M.W.G. by the Gruber foundation, and R.G. by a MITACS Accélération postdoctoral fellowship. The funders had no role in study design, data collection and analysis, decision to publish, or preparation of the manuscript.

AUTHOR CONTRIBUTIONS

Conceptualization, W.L., Y.C., J.P., M.P., A.F., and W.M.; investigation, W.L., Y.C., J.P., I.U., M.L., S.Y.G., A.T., R.G., D.V., S.P.A., G.G., D.C., S.D., W.D.T., M.W.G., S.Z., J.R., F.Z., R.K.H., L.E., A.Z., and P.D.U.; resources, Y.B. and M.C.; writing—original draft, W.L. and W.M.; writing—review and editing, W.L., Y.C., J.P., M.P., A.F., and W.M.; supervision, M.C., P.K., J.S., D.X., P.D.U., M.P., A.F., and W.M.; funding acquisition, M.P., A.F., and W.M.

DECLARATION OF INTERESTS

The authors declare no competing interests.

Received: August 27, 2021
Revised: October 26, 2021
Accepted: December 13, 2021
Published: January 11, 2022

REFERENCES

Anand, S.P., Chen, Y., Prévost, J., Gasser, R., Beaudoin-Bussières, G., Abrams, C.F., Pazgier, M., and Finzi, A. (2020). Interaction of human ACE2 to membrane-bound SARS-CoV-1 and SARS-CoV-2 S glycoproteins. Viruses *12*, 1104.

Anthony, S.J., Gilardi, K., Menachery, V.D., Goldstein, T., Ssebide, B., Mbabazi, R., Navarrete-Macias, I., Liang, E., Wells, H., Hicks, A., et al. (2017). Further evidence for bats as the evolutionary Source of Middle East respiratory syndrome coronavirus. mBio *8*, e00373–00317.

Baden, L.R., El Sahly, H.M., Essink, B., Kotloff, K., Frey, S., Novak, R., Diemert, D., Spector, S.A., Rouphael, N., Creech, C.B., et al. (2020). Efficacy and safety of the mRNA-1273 SARS-CoV-2 vaccine. New Engl. J. Med. *384*, 403–416.

Barad, B.A., Echols, N., Wang, R.Y.-R., Cheng, Y., DiMaio, F., Adams, P.D., and Fraser, J.S. (2015). EMRinger: side chain–directed model and map validation for 3D cryo-electron microscopy. Nat. Methods *12*, 943–946.

Barnes, C.O., West, A.P., Jr., Huey-Tubman, K.E., Hoffmann, M.A.G., Sharaf, N.G., Hoffman, P.R., Koranda, N., Gristick, H.B., Gaebler, C., Muecksch, F., et al. (2020). Structures of human antibodies bound to SARS-CoV-2 spike reveal common epitopes and recurrent features of antibodies. Cell *182*, 828–842.e816.

Beaudoin-Bussières, G., Laumaea, A., Anand, S.P., Prévost, J., Gasser, R., Goyette, G., Medjahed, H., Perreault, J., Tremblay, T., Lewin, A., et al. (2020). Decline of humoral responses against SARS-CoV-2 spike in convalescent individuals. mBio *11*, e02590–02520.

Burnley, T., Palmer, C.M., and Winn, M. (2017). Recent developments in the CCP-EM software suite. Acta Crystallogr. Section D *73*, 469–477.

Cai, Y., Zhang, J., Xiao, T., Peng, H., Sterling, S.M., Walsh, R.M., Rawson, S., Rits-Volloch, S., and Chen, B. (2020). Distinct conformational states of SARS-CoV-2 spike protein. Science *369*, 1586–1592.

Campbell, F., Archer, B., Laurenson-Schafer, H., Jinnai, Y., Konings, F., Batra, N., Pavlin, B., Vandemaele, K., Van Kerkhove, M.D., Jombart, T., et al. (2021). Increased transmissibility and global spread of SARS-CoV-2 variants of concern as at June 2021. Eurosurveillance *26*, 2100509.

Chen, C., Boorla, V.S., Banerjee, D., Chowdhury, R., Cavener, V.S., Nissly, R.H., Gontu, A., Boyle, N.R., Vandegrift, K., Nair, M.S., et al. (2021). Computational prediction of the effect of amino acid changes on the binding affinity between SARS-CoV-2 spike RBD and human ACE2. Proc. Natl. Acad. Sci *118*, e2106480118.

Chen, V.B., Arendall, W.B., III, Headd, J.J., Keedy, D.A., Immormino, R.M., Kapral, G.J., Murray, L.W., Richardson, J.S., and Richardson, D.C. (2010). MolProbity: all-atom structure validation for macromolecular crystallography. Acta Crystallogr. Section D *66*, 12–21.

Dejnirattisai, W., Zhou, D., Ginn, H.M., Duyvesteyn, H.M.E., Supasa, P., Case, J.B., Zhao, Y., Walter, T.S., Mentzer, A.J., Liu, C., et al. (2021). The antigenic anatomy of SARS-CoV-2 receptor binding domain. Cell *184*, 2183–2200.e2122.

Dieterle, M.E., Haslwanter, D., Bortz, R.H., Wirchnianski, A.S., Lasso, G., Vergnolle, O., Abbasi, S.A., Fels, J.M., Laudermilch, E., Florez, C., et al. (2020). A replication-competent vesicular stomatitis virus for studies of SARS-CoV-2 spike-mediated cell entry and its inhibition. Cell Host & Microbe *28*, 486–496.e486.

Dong, E., Du, H., and Gardner, L. (2020). An interactive web-based dashboard to track COVID-19 in real time. Lancet Infect. Dis. *20*, 533–534.

Du, S., Liu, P., Zhang, Z., Xiao, T., Yasimayi, A., Huang, W., Wang, Y., Cao, Y., Xie, X.S., and Xiao, J. (2021). Structures of SARS-CoV-2 B.1.351 neutralizing antibodies provide insights into cocktail design against concerning variants. Cell Res. *31*, 1130–1133.

Dunbar, J., Krawczyk, K., Leem, J., Marks, C., Nowak, J., Regep, C., Georges, G., Kelm, S., Popovic, B., and Deane, C.M. (2016). SAbPred: a structure-based antibody prediction server. Nucleic Acids Res. *44*, W474–W478.

Emsley, P., and Cowtan, K. (2004). Coot: model-building tools for molecular graphics. Acta Crystallogr. D Biol. Crystallogr. *60*, 2126–2132.

Folegatti, P.M., Ewer, K.J., Aley, P.K., Angus, B., Becker, S., Belij-Rammerstorfer, S., Bellamy, D., Bibi, S., Bittaye, M., Clutterbuck, E.A., et al. (2020). Safety and immunogenicity of the ChAdOx1 nCoV-19 vaccine against SARS-CoV-2: a preliminary report of a phase 1/2, single-blind, randomised controlled trial. The Lancet *396*, 467–478.

Ge, J., Wang, R., Ju, B., Zhang, Q., Sun, J., Chen, P., Zhang, S., Tian, Y., Shan, S., Cheng, L., et al. (2021). Antibody neutralization of SARS-CoV-2 through ACE2 receptor mimicry. Nat. Commun. *12*, 250.

Ge, X.-Y., Li, J.-L., Yang, X.-L., Chmura, A.A., Zhu, G., Epstein, J.H., Mazet, J.K., Hu, B., Zhang, W., Peng, C., et al. (2013). Isolation and characterization of a bat SARS-like coronavirus that uses the ACE2 receptor. Nature *503*, 535–538.

Gobeil, S.M.C., Janowska, K., McDowell, S., Mansouri, K., Parks, R., Stalls, V., Kopp, M.F., Manne, K., Li, D., Wiehe, K., et al. (2021). Effect of natural mutations of SARS-CoV-2 on spike structure, conformation, and antigenicity. Scienceeabi6226.

Goddard, T.D., Huang, C.C., Meng, E.C., Pettersen, E.F., Couch, G.S., Morris, J.H., and Ferrin, T.E. (2018). UCSF ChimeraX: Meeting modern challenges in visualization and analysis. Protein Sci. *27*, 14–25.

Greaney, A.J., Loes, A.N., Crawford, K.H.D., Starr, T.N., Malone, K.D., Chu, H.Y., and Bloom, J.D. (2021a). Comprehensive mapping of mutations in the SARS-CoV-2 receptor-binding domain that affect recognition by polyclonal human plasma antibodies. Cell Host & Microbe *29*, 463–476.e466.

Greaney, A.J., Starr, T.N., Gilchuk, P., Zost, S.J., Binshtein, E., Loes, A.N., Hilton, S.K., Huddleston, J., Eguia, R., Crawford, K.H.D., et al. (2021b). Complete mapping of mutations to the SARS-CoV-2 spike receptor-binding domain that escape antibody recognition. Cell Host & Microbe *29*, 44–57.e49.

Grifoni, A., Sidney, J., Zhang, Y., Scheuermann, R.H., Peters, B., and Sette, A. (2020). A sequence homology and bioinformatic approach can predict candidate targets for immune responses to SARS-CoV-2. Cell Host & Microbe *27*, 671–680.e672.

Hagen, W.J.H., Wan, W., and Briggs, J.A.G. (2017). Implementation of a cryo-electron tomography tilt-scheme optimized for high resolution subtomogram averaging. J. Struct. Biol. *197*, 191–198.

Hastie, K.M., Li, H., Bedinger, D., Schendel, S.L., Dennison, S.M., Li, K., Rayaprolu, V., Yu, X., Mann, C., Zandonatti, M., et al. (2021). Defining variant-resistant epitopes targeted by SARS-CoV-2 antibodies: A global consortium study. Science *374*, 472–478.

Hoffmann, M., Arora, P., Groß, R., Seidel, A., Hörnich, B.F., Hahn, A.S., Krüger, N., Graichen, L., Hofmann-Winkler, H., Kempf, A., et al. (2021). SARS-CoV-2 variants B.1.351 and P.1 escape from neutralizing antibodies. Cell *184*, 2384–2393.e2312.

Hoffmann, M., Kleine-Weber, H., Schroeder, S., Krüger, N., Herrler, T., Erichsen, S., Schiergens, T.S., Herrler, G., Wu, N.-H., Nitsche, A., et al. (2020). SARS-CoV-2 cell entry depends on ACE2 and TMPRSS2 and is blocked by a clinically proven protease inhibitor. Cell *181*, 271–280.e278.

Hsieh, C.-L., Goldsmith, J.A., Schaub, J.M., DiVenere, A.M., Kuo, H.-C., Javanmardi, K., Le, K.C., Wrapp, D., Lee, A.G., Liu, Y., et al. (2020). Structure-based design of prefusion-stabilized SARS-CoV-2 spikes. Science *369*, 1501.

Hurlburt, N.K., Homad, L.J., Sinha, I., Jennewein, M.F., MacCamy, A.J., Wan, Y.-H., Boonyaratanakornkit, J., Sholukh, A.M., Zhou, P., Burton, D.R., et al. (2021). Structural definition of a pan-sarbecovirus neutralizing epitope on the spike S2 subunit. bioRxiv. https://doi.org/10.1101/2021.08.02.454829.

Jennewein, M.F., MacCamy, A.J., Akins, N.R., Feng, J., Homad, L.J., Hurlburt, N.K., Seydoux, E., Wan, Y.-H., Stuart, A.B., Edara, V.V., et al. (2021). Isolation and characterization of cross-neutralizing coronavirus antibodies from COVID-19 + subjects. Cell Rep. *36*, 109353.

Jette, C.A., Cohen, A.A., Gnanapragasam, P.N.P., Muecksch, F., Lee, Y.E., Huey-Tubman, K.E., Schmidt, F., Hatziioannou, T., Bieniasz, P.D., Nussenzweig, M.C., et al. (2021). Broad cross-reactivity across sarbecoviruses exhibited by a subset of COVID-19 donor-derived neutralizing antibodies. Cell Rep. *36*, 109760.

Ju, B., Zhang, Q., Ge, J., Wang, R., Sun, J., Ge, X., Yu, J., Shan, S., Zhou, B., Song, S., et al. (2020). Human neutralizing antibodies elicited by SARS-CoV-2 infection. Nature *584*, 115–119.

Juette, M.F., Terry, D.S., Wasserman, M.R., Altman, R.B., Zhou, Z., Zhao, H., and Blanchard, S.C. (2016). Single-molecule imaging of non-equilibrium molecular ensembles on the millisecond timescale. Nature Methods *13*, 341–344.

Ke, Z., Oton, J., Qu, K., Cortese, M., Zila, V., McKeane, L., Nakane, T., Zivanov, J., Neufeldt, C.J., Cerikan, B., et al. (2020). Structures and distributions of SARS-CoV-2 spike proteins on intact virions. Nature *588*, 498–502.

Krissinel, E., and Henrick, K. (2007). Inference of macromolecular assemblies from crystalline state. J. Mol. Biol. *372*, 774–797.

Lan, J., Ge, J., Yu, J., Shan, S., Zhou, H., Fan, S., Zhang, Q., Shi, X., Wang, Q., Zhang, L., et al. (2020). Structure of the SARS-CoV-2 spike receptor-binding domain bound to the ACE2 receptor. Nature *581*, 215–220.

Laumaea, A., Smith, A.B., III, Sodroski, J., and Finzi, A. (2020). Opening the HIV envelope: potential of CD4 mimics as multifunctional HIV entry inhibitors. Curr. Opin. HIV AIDS *15*, 300–308.

Letko, M., Marzi, A., and Munster, V. (2020). Functional assessment of cell entry and receptor usage for SARS-CoV-2 and other lineage B betacoronaviruses. Nat. Microbiol. *5*, 562–569.

Li, T., Han, X., Gu, C., Guo, H., Zhang, H., Wang, Y., Hu, C., Wang, K., Liu, F., Luo, F., et al. (2021a). Potent SARS-CoV-2 neutralizing antibodies with protective efficacy against newly emerged mutational variants. Nat. Commun. *12*, 6304.

Li, T., Xue, W., Zheng, Q., Song, S., Yang, C., Xiong, H., Zhang, S., Hong, M., Zhang, Y., Yu, H., et al. (2021b). Cross-neutralizing antibodies bind a SARS-CoV-2 cryptic site and resist circulating variants. Nat. Commun. *12*, 5652.

Li, W., Moore, M.J., Vasilieva, N., Sui, J., Wong, S.K., Berne, M.A., Somasundaran, M., Sullivan, J.L., Luzuriaga, K., Greenough, T.C., et al. (2003). Angiotensin-converting enzyme 2 is a functional receptor for the SARS coronavirus. Nature *426*, 450–454.

Li, Z., Li, W., Lu, M., Bess, J., Chao, C.W., Gorman, J., Terry, D.S., Zhang, B., Zhou, T., Blanchard, S.C., et al. (2020). Subnanometer structures of HIV-1 envelope trimers on aldrithiol-2-inactivated virus particles. Nat. Struct. Mol. Biol. *27*, 726–734.

Liebschner, D., Afonine, P.V., Baker, M.L., Bunkoczi, G., Chen, V.B., Croll, T.I., Hintze, B., Hung, L.W., Jain, S., McCoy, A.J., et al. (2019). Macromolecular structure determination using X-rays, neutrons and electrons: recent developments in Phenix. Acta Crystallogr. D Struct. Biol. *75*, 861–877.

Liu, L., Wang, P., Nair, M.S., Yu, J., Rapp, M., Wang, Q., Luo, Y., Chan, J.F.W., Sahi, V., Figueroa, A., et al. (2020). Potent neutralizing antibodies against multiple epitopes on SARS-CoV-2 spike. Nature *584*, 450–456.

Liu, Z., VanBlargan, L.A., Bloyet, L.-M., Rothlauf, P.W., Chen, R.E., Stumpf, S., Zhao, H., Errico, J.M., Theel, E.S., Liebeskind, M.J., et al. (2021). Identification of SARS-CoV-2 spike mutations that attenuate monoclonal and serum antibody neutralization. Cell Host & Microbe *29*, 477–488.e474.

Logunov, D.Y., Dolzhikova, I.V., Shcheblyakov, D.V., Tukhvatulin, A.I., Zubkova, O.V., Dzharullaeva, A.S., Kovyrshina, A.V., Lubenets, N.L., Grousova, D.M., Erokhova, A.S., et al. (2021). Safety and efficacy of an rAd26 and rAd5 vector-based heterologous prime-boost COVID-19 vaccine: an interim analysis of a randomised controlled phase 3 trial in Russia. The Lancet *397*, 671–681.

Long, Y., Song, S., Luo, F., Han, X., Hu, C., Wang, Y., Li, S., Wang, W., Zhang, H., Zhang, B., et al. (2021). A non-RBM targeted RBD specific antibody neutralizes SARS-CoV-2 inducing S1 shedding. Biochem. Biophysical Res. Commun. *571*, 152–158.

Lopéz-Blanco, J.R., and Chacón, P. (2013). iMODFIT: Efficient and robust flexible fitting based on vibrational analysis in internal coordinates. J. Struct. Biol. *184*, 261–270.

Lu, M., Ma, X., Castillo-Menedez, L.R., Gorman, J., Alsahafi, N., Ermel, U., Terry, D.S., Chambers, M., Peng, D., Zhang, B., et al. (2019). Associating HIV-1 envelope glycoprotein structures with states on the virus observed by smFRET. Nature *568*, 415–419.

Lu, M., Uchil, P.D., Li, W., Zheng, D., Terry, D.S., Gorman, J., Shi, W., Zhang, B., Zhou, T., Ding, S., et al. (2020). Real-time conformational dynamics of SARS-CoV-2 spikes on virus particles. Cell Host & Microbe *28*, 880–891.e888.

Ma, Z., Li, P., Ji, Y., Ikram, A., and Pan, Q. (2020). Cross-reactivity towards SARS-CoV-2: the potential role of low-pathogenic human coronaviruses. The Lancet Microbe *1*, e151.

Mastronarde, D.N. (2005). Automated electron microscope tomography using robust prediction of specimen movements. J. Struct. Biol. *152*, 36–51.

Mastronarde, D.N., and Held, S.R. (2017). Automated tilt series alignment and tomographic reconstruction in IMOD. J. Struct. Biol. *197*, 102–113.

McCallum, M., De Marco, A., Lempp, F.A., Tortorici, M.A., Pinto, D., Walls, A.C., Beltramello, M., Chen, A., Liu, Z., Zatta, F., et al. (2021). N-terminal domain antigenic mapping reveals a site of vulnerability for SARS-CoV-2. Cell *184*, 2332–2347.e2316.

Menachery, V.D., Yount, B.L., Debbink, K., Agnihothram, S., Gralinski, L.E., Plante, J.A., Graham, R.L., Scobey, T., Ge, X.-Y., Donaldson, E.F., et al. (2015). A SARS-like cluster of circulating bat coronaviruses shows potential for human emergence. Nat. Med. *21*, 1508–1513.

Menachery, V.D., Yount, B.L., Sims, A.C., Debbink, K., Agnihothram, S.S., Gralinski, L.E., Graham, R.L., Scobey, T., Plante, J.A., Royal, S.R., et al. (2016). SARS-like WIV1-CoV poised for human emergence. Proc. Natl. Acad. Sci. *113*, 3048.

Minor, W., Cymborowski, M., Otwinowski, Z., and Chruszcz, M. (2006). HKL-3000: the integration of data reduction and structure solution–from diffraction images to an initial model in minutes. Acta Crystallogr. D Biol. Crystallogr. *62*, 859–866.

Montefiori, D.C., and Acharya, P. (2021). SnapShot: SARS-CoV-2 antibodies. Cell Host & Microbe *29*, 1162–1162.e1161.

Munro, J.B., Gorman, J., Ma, X., Zhou, Z., Arthos, J., Burton, D.R., Koff, W.C., Courter, J.R., Smith, A.B., Kwong, P.D., et al. (2014). Conformational dynamics of single HIV-1 envelope trimers on the surface of native virions. Science *346*, 759–763.

Ng, K.W., Faulkner, N., Cornish, G.H., Rosa, A., Harvey, R., Hussain, S., Ulferts, R., Earl, C., Wrobel, A.G., Benton, D.J., et al. (2020). Preexisting and de novo humoral immunity to SARS-CoV-2 in humans. Science *370*, 1339.

Nguyen, H.T., Zhang, S., Wang, Q., Anang, S., Wang, J., Ding, H., Kappes, J.C., Sodroski, J., and Dutch, R.E. (2021). Spike glycoprotein and host cell determinants of SARS-CoV-2 entry and cytopathic effects. J. Virol. *95*, e02304–e02320.

Ou, X., Liu, Y., Lei, X., Li, P., Mi, D., Ren, L., Guo, L., Guo, R., Chen, T., Hu, J., et al. (2020). Characterization of spike glycoprotein of SARS-CoV-2 on virus entry and its immune cross-reactivity with SARS-CoV. Nat. Commun. *11*, 1620.

Pettersen, E.F., Goddard, T.D., Huang, C.C., Couch, G.S., Greenblatt, D.M., Meng, E.C., and Ferrin, T.E. (2004). UCSF Chimera—a visualization system for exploratory research and analysis. J. Comput. Chem. *25*, 1605–1612.

Pettersen, E.F., Goddard, T.D., Huang, C.C., Meng, E.C., Couch, G.S., Croll, T.I., Morris, J.H., and Ferrin, T.E. (2021). UCSF ChimeraX: Structure visualization for researchers, educators, and developers. Protein Sci. *30*, 70–82.

Pinto, D., Sauer Maximilian, M., Czudnochowski, N., Low Jun, S., Tortorici, M.A., Housley Michael, P., Noack, J., Walls Alexandra, C., Bowen John, E., Guarino, B., et al. (2021). Broad betacoronavirus neutralization by a stem helix–specific human antibody. Science *373*, 1109–1116.

Planas, D., Bruel, T., Grzelak, L., Guivel-Benhassine, F., Staropoli, I., Porrot, F., Planchais, C., Buchrieser, J., Rajah, M.M., Bishop, E., et al. (2021a). Sensitivity of infectious SARS-CoV-2 B.1.1.7 and B.1.351 variants to neutralizing antibodies. Nat. Med. *27*, 917–924.

Planas, D., Veyer, D., Baidaliuk, A., Staropoli, I., Guivel-Benhassine, F., Rajah, M.M., Planchais, C., Porrot, F., Robillard, N., Puech, J., et al. (2021b). Reduced sensitivity of SARS-CoV-2 variant Delta to antibody neutralization. Nature *596*, 276–280.

Polack, F.P., Thomas, S.J., Kitchin, N., Absalon, J., Gurtman, A., Lockhart, S., Perez, J.L., Pérez Marc, G., Moreira, E.D., Zerbini, C., et al. (2020). Safety and efficacy of the BNT162b2 mRNA covid-19 vaccine. New Engl. J. Med. *383*, 2603–2615.

Prévost, J., and Finzi, A. (2021). The great escape? SARS-CoV-2 variants evading neutralizing responses. Cell Host & Microbe *29*, 322–324.

Prévost, J., Gasser, R., Beaudoin-Bussières, G., Richard, J., Duerr, R., Laumaea, A., Anand, S.P., Goyette, G., Benlarbi, M., Ding, S., et al. (2020). Cross-sectional evaluation of humoral responses against SARS-CoV-2 spike. Cell Rep. Med *1*, 100126.

Punjani, A., Rubinstein, J.L., Fleet, D.J., and Brubaker, M.A. (2017). cryoSPARC: algorithms for rapid unsupervised cryo-EM structure determination. Nat. Methods *14*, 290–296.

Rappazzo, C.G., Tse Longping, V., Kaku Chengzi, I., Wrapp, D., Sakharkar, M., Huang, D., Deveau Laura, M., Yockachonis Thomas, J., Herbert Andrew, S., Battles Michael, B., et al. (2021). Broad and potent activity against SARS-like viruses by an engineered human monoclonal antibody. Science *371*, 823–829.

Robbiani, D.F., Gaebler, C., Muecksch, F., Lorenzi, J.C.C., Wang, Z., Cho, A., Agudelo, M., Barnes, C.O., Gazumyan, A., Finkin, S., et al. (2020). Convergent antibody responses to SARS-CoV-2 in convalescent individuals. Nature *584*, 437–442.

Rubinstein, J.L., and Brubaker, M.A. (2015). Alignment of cryo-EM movies of individual particles by optimization of image translations. J. Struct. Biol. *192*, 188–195.

Sadoff, J., Gray, G., Vandebosch, A., Cárdenas, V., Shukarev, G., Grinsztejn, B., Goepfert, P.A., Truyers, C., Fennema, H., Spiessens, B., et al. (2021a).

Safety and efficacy of single-dose Ad26.COV2.S vaccine against covid-19. New Engl. J. Med. *384*, 2187–2201.

Sadoff, J., Le Gars, M., Shukarev, G., Heerwegh, D., Truyers, C., de Groot, A.M., Stoop, J., Tete, S., Van Damme, W., Leroux-Roels, I., et al. (2021b). Interim results of a phase 1–2a trial of Ad26.COV2.S covid-19 vaccine. New Engl. J. Med. *384*, 1824–1835.

Sauer, M.M., Tortorici, M.A., Park, Y.-J., Walls, A.C., Homad, L., Acton, O.J., Bowen, J.E., Wang, C., Xiong, X., de van der Schueren, W., et al. (2021). Structural basis for broad coronavirus neutralization. Nat. Struct. Mol. Biol. *28*, 478–486.

Schmidt, F., Weisblum, Y., Muecksch, F., Hoffmann, H.-H., Michailidis, E., Lorenzi, J.C.C., Mendoza, P., Rutkowska, M., Bednarski, E., Gaebler, C., et al. (2020). Measuring SARS-CoV-2 neutralizing antibody activity using pseudotyped and chimeric virusesSARS-CoV-2 neutralizing antibody activity. J. Exp. Med *217*, e20201181.

Shang, J., Ye, G., Shi, K., Wan, Y., Luo, C., Aihara, H., Geng, Q., Auerbach, A., and Li, F. (2020). Structural basis of receptor recognition by SARS-CoV-2. Nature *581*, 221–224.

Skowronski, D.M., Setayeshgar, S., Zou, M., Prystajecky, N., Tyson, J.R., Galanis, E., Naus, M., Patrick, D.M., Sbihi, H., El Adam, S., et al. (2021). Single-dose mRNA vaccine effectiveness against SARS-CoV-2, including Alpha and Gamma variants: a test-negative design in adults 70 years and older in British Columbia, Canada. Clin. Infect. Disciab616.

Song, G., He, W.-t., Callaghan, S., Anzanello, F., Huang, D., Ricketts, J., Torres, J.L., Beutler, N., Peng, L., Vargas, S., et al. (2021). Cross-reactive serum and memory B-cell responses to spike protein in SARS-CoV-2 and endemic coronavirus infection. Nat. Commun. *12*, 2938.

Starr, T.N., Greaney, A.J., Addetia, A., Hannon, W.W., Choudhary, M.C., Dingens, A.S., Li, J.Z., and Bloom, J.D. (2021). Prospective mapping of viral mutations that escape antibodies used to treat COVID-19. Science *371*, 850.

Starr, T.N., Greaney, A.J., Hilton, S.K., Ellis, D., Crawford, K.H.D., Dingens, A.S., Navarro, M.J., Bowen, J.E., Tortorici, M.A., Walls, A.C., et al. (2020). Deep mutational scanning of SARS-CoV-2 receptor binding domain reveals constraints on folding and ACE2 binding. Cell *182*, 1295–1310.e1220.

Tauzin, A., Nayrac, M., Benlarbi, M., Gong, S.Y., Gasser, R., Beaudoin-Bussières, G., Brassard, N., Laumaea, A., Vézina, D., Prévost, J., et al. (2021). A single dose of the SARS-CoV-2 vaccine BNT162b2 elicits Fc-mediated antibody effector functions and T cell responses. Cell Host & Microbe *29*, 1137–1150.e1136.

Tian, X., Li, C., Huang, A., Xia, S., Lu, S., Shi, Z., Lu, L., Jiang, S., Yang, Z., Wu, Y., et al. (2020). Potent binding of 2019 novel coronavirus spike protein by a SARS coronavirus-specific human monoclonal antibody. Emerging Microbes & Infections *9*, 382–385.

Tortorici, M.A., Beltramello, M., Lempp Florian, A., Pinto, D., Dang Ha, V., Rosen Laura, E., McCallum, M., Bowen, J., Minola, A., Jaconi, S., et al. (2020). Ultrapotent human antibodies protect against SARS-CoV-2 challenge via multiple mechanisms. Science *370*, 950–957.

Tortorici, M.A., Czudnochowski, N., Starr, T.N., Marzi, R., Walls, A.C., Zatta, F., Bowen, J.E., Jaconi, S., Di Iulio, J., Wang, Z., et al. (2021). Broad sarbecovirus neutralization by a human monoclonal antibody. Nature *597*, 103–108.

Turoňová, B., Sikora, M., Schürmann, C., Hagen, W.J.H., Welsch, S., Blanc, F.E.C., von Bülow, S., Gecht, M., Bagola, K., Hörner, C., et al. (2020). In situ structural analysis of SARS-CoV-2 spike reveals flexibility mediated by three hinges. Science *370*, 203.

Ullah, I., Prévost, J., Ladinsky, M.S., Stone, H., Lu, M., Anand, S.P., Beaudoin-Bussières, G., Symmes, K., Benlarbi, M., Ding, S., et al. (2021). Live imaging of SARS-CoV-2 infection in mice reveals that neutralizing antibodies require Fc function for optimal efficacy. Immunity *54*, 2143–2158.e2115.

Volz, E., Mishra, S., Chand, M., Barrett, J.C., Johnson, R., Geidelberg, L., Hinsley, W.R., Laydon, D.J., Dabrera, G., O'Toole, Á., et al. (2021). Assessing transmissibility of SARS-CoV-2 lineage B.1.1.7 in England. Nature *593*, 266–269.

Voysey, M., Clemens, S.A.C., Madhi, S.A., Weckx, L.Y., Folegatti, P.M., Aley, P.K., Angus, B., Baillie, V.L., Barnabas, S.L., Bhorat, Q.E., et al. (2021). Safety and efficacy of the ChAdOx1 nCoV-19 vaccine (AZD1222) against SARS-CoV-2: an interim analysis of four randomised controlled trials in Brazil, South Africa, and the UK. The Lancet *397*, 99–111.

Walls, A.C., Park, Y.-J., Tortorici, M.A., Wall, A., McGuire, A.T., and Veesler, D. (2020). Structure, function, and antigenicity of the SARS-CoV-2 spike glycoprotein. Cell *181*, 281–292.e286.

Walls, A.C., Xiong, X., Park, Y.-J., Tortorici, M.A., Snijder, J., Quispe, J., Cameroni, E., Gopal, R., Dai, M., Lanzavecchia, A., et al. (2019). Unexpected receptor functional mimicry elucidates activation of coronavirus fusion. Cell *176*, 1026–1039.e1015.

Wang, C., Li, W., Drabek, D., Okba, N.M.A., van Haperen, R., Osterhaus, A.D.M.E., van Kuppeveld, F.J.M., Haagmans, B.L., Grosveld, F., and Bosch, B.-J. (2020). A human monoclonal antibody blocking SARS-CoV-2 infection. Nat. Commun. *11*, 2251.

Wang, C., van Haperen, R., Gutiérrez-Álvarez, J., Li, W., Okba, N.M.A., Albulescu, I., Widjaja, I., van Dieren, B., Fernandez-Delgado, R., Sola, I., et al. (2021a). A conserved immunogenic and vulnerable site on the coronavirus spike protein delineated by cross-reactive monoclonal antibodies. Nat. Commun. *12*, 1715.

Wang, L., Zhou, T., Zhang, Y., Yang Eun, S., Schramm Chaim, A., Shi, W., Pegu, A., Oloniniyi Olamide, K., Henry Amy, R., Darko, S., et al. (2021b). Ultrapotent antibodies against diverse and highly transmissible SARS-CoV-2 variants. Science *373*, eabh1766.

Wang, N., Li, S.-Y., Yang, X.-L., Huang, H.-M., Zhang, Y.-J., Guo, H., Luo, C.-M., Miller, M., Zhu, G., Chmura, A.A., et al. (2018). Serological evidence of bat SARS-related coronavirus infection in humans, China. Virologica Sinica *33*, 104–107.

Wec Anna, Z., Wrapp, D., Herbert Andrew, S., Maurer Daniel, P., Haslwanter, D., Sakharkar, M., Jangra Rohit, K., Dieterle, M.E., Lilov, A., Huang, D., et al. (2020). Broad neutralization of SARS-related viruses by human monoclonal antibodies. Science *369*, 731–736.

Weisblum, Y., Schmidt, F., Zhang, F., DaSilva, J., Poston, D., Lorenzi, J.C.C., Muecksch, F., Rutkowska, M., Hoffmann, H.-H., Michailidis, E., et al. (2020). Escape from neutralizing antibodies by SARS-CoV-2 spike protein variants. eLife *9*, e61312.

Winkler, H. (2007). 3D reconstruction and processing of volumetric data in cryo-electron tomography. J. Struct. Biol. *157*, 126–137.

Wrapp, D., Wang, N., Corbett, K.S., Goldsmith, J.A., Hsieh, C.-L., Abiona, O., Graham, B.S., and McLellan, J.S. (2020). Cryo-EM structure of the 2019-nCoV spike in the prefusion conformation. Science *367*, 1260.

Xiao, T., Lu, J., Zhang, J., Johnson, R.I., McKay, L.G.A., Storm, N., Lavine, C.L., Peng, H., Cai, Y., Rits-Volloch, S., et al. (2021). A trimeric human angiotensin-converting enzyme 2 as an anti-SARS-CoV-2 agent. Nat. Struct. Mol. Biol. *28*, 202–209.

Xu, C., Wang, Y., Liu, C., Zhang, C., Han, W., Hong, X., Wang, Y., Hong, Q., Wang, S., Zhao, Q., et al. (2021). Conformational dynamics of SARS-CoV-2 trimeric spike glycoprotein in complex with receptor ACE2 revealed by cryo-EM. Sci. Adv *7*, eabe5575.

Yamamoto, M., Du, Q., Song, J., Wang, H., Watanabe, A., Tanaka, Y., Kawaguchi, Y., Inoue, J.-i., and Matsuda, Z. (2019). Cell–cell and virus–cell fusion assay–based analyses of alanine insertion mutants in the distal α9 portion of the JRFL gp41 subunit from HIV-1. J. Biol. Chem. *294*, 5677–5687.

Yao, H., Song, Y., Chen, Y., Wu, N., Xu, J., Sun, C., Zhang, J., Weng, T., Zhang, Z., Wu, Z., et al. (2020). Molecular architecture of the SARS-CoV-2 virus. Cell *183*, 730–738.e13.

Yu, J., Li, Z., He, X., Gebre Makda, S., Bondzie Esther, A., Wan, H., Jacob-Dolan, C., Martinez David, R., Nkolola Joseph, P., Baric Ralph, S., et al. (2021). Deletion of the SARS-CoV-2 spike cytoplasmic tail increases infectivity in pseudovirus neutralization assays. J. Virol. *95*, e00044–00021.

Zheng, S.Q., Palovcak, E., Armache, J.-P., Verba, K.A., Cheng, Y., and Agard, D.A. (2017). MotionCor2: anisotropic correction of beam-induced

motion for improved cryo-electron microscopy. Nat. Methods *14*, 331–332.

Zhou, P., Yang, X.-L., Wang, X.-G., Hu, B., Zhang, L., Zhang, W., Si, H.-R., Zhu, Y., Li, B., Huang, C.-L., et al. (2020). A pneumonia outbreak associated with a new coronavirus of probable bat origin. Nature *579*, 270–273.

Zhou, P., Yuan, M., Song, G., Beutler, N., Shaabani, N., Huang, D., He, W.-t., Zhu, X., Callaghan, S., Yong, P., et al. (2021). A protective broadly cross-reactive human antibody defines a conserved site of vulnerability on beta-coronavirus spikes. bioRxiv. https://doi.org/10.1101/2021.03.30.437769.

Zhu, N., Zhang, D., Wang, W., Li, X., Yang, B., Song, J., Zhao, X., Huang, B., Shi, W., Lu, R., et al. (2020). A novel coronavirus from patients with pneumonia in China, 2019. New Engl. J. Med. *382*, 727–733.

Zost, S.J., Gilchuk, P., Case, J.B., Binshtein, E., Chen, R.E., Nkolola, J.P., Schäfer, A., Reidy, J.X., Trivette, A., Nargi, R.S., et al. (2020). Potently neutralizing and protective human antibodies against SARS-CoV-2. Nature *584*, 443–449.

STAR★METHODS

KEY RESOURCES TABLE

REAGENT or RESOURCE	SOURCE	IDENTIFIER
Antibodies		
CV3-1	Jennewein et al. 2021	NA
CV3-25	Jennewein et al. 2021	NA
CV3-25 GASDALIE	Ullah et al. 2021	N/A
Rabbit anti-SARS-CoV-2 RBD polyclonal antibody	This paper	N/A
Goat anti-Human IgG (H + L) Cross-Adsorbed Secondary Antibody, Alexa Fluor 647	Invitrogen	Cat # A-21445; RRID: AB_2535862
Goat anti-Human IgG Fc Cross-Adsorbed Secondary Antibody, HRP	Invitrogen	Cat # A18823; RRID: AB_2535600
Bacterial and virus strains		
SARS-CoV-2, Isolate hCoV-19/USA/MD-HP01542/2021	BEI Resources	Cat # NR-55282
Chemicals, peptides, and recombinant proteins		
Dulbecco's modified Eagle's medium (DMEM)	Wisent	Cat# 319-005-CL
Gibco™ RPMI 1640 medium	Thermo Fisher Scientific	Cat # 11875093
Penicillin/streptomycin	Wisent	Cat# 450-201-EL
Fetal bovine serum (FBS)	VWR	Cat# 97068-085
Gibco™ DMEM, high glucose, without L-Gln, L-Met and L-Cys	Thermo Fisher Scientific	Cat # 21013024
Gibco™ GlutaMax™ (100X)	Thermo Fisher Scientific	Cat #35050061
Gibco™ Dialyzed FBS	Thermo Fisher Scientific	Cat # 26400036
Bovine Serum Albumin (BSA)	Bioshop	Cat # ALB001.100
EDTA 0.5 M pH 8.0	Invitrogen	Cat # 15575020
Phosphate-buffered saline (PBS)	Wisent	Cat #311-010-1L
Tris-buffered saline (TBS)	ThermoFisher Scientific	Cat # BP24711
Western Lightning Plus-ECL, Enhanced Chemiluminescence Substrate	Perkin Elmer Life Sciences	Cat # NEL105001EA
Tween 20	Thermo Fisher Scientific	Cat # BP337-500
Passive lysis buffer	Promega	Cat # E1941
Sodium chloride (NaCl)	Bioshop	Cat # SOD001.10
Sodium Phosphate Monobasic Anhydrous (NaH_2PO_4)	Fisher Scientific	Cat # BP329-1
Sodium Phosphate Dibasic Anhydrous (Na_2HPO_4)	Fisher Scientific	Cat #S374-1
Sodium dodecyl sulfate (SDS)	Fisher Scientific	Cat # BP166-500
Sodium deoxycholate (DOC)	Sigma-Aldrich	Cat # 30970-100G
Pierce™ Protease inhibitor Tablets	ThermoFisher Scientific	Cat # A32963
Avicel® Pharma Grade	FMC	Cat # RC-581 NF 10.20944/preprints202005.0264.v1
Magnesium sulfate heptahydrate ($MgSO_4 \cdot 7H_20$)	Bioshop	Cat # MAG511.500
Potassium dihydrogen phosphate (KH_2PO_4)	Fisher Scientific	Cat # BP362-1
Adenosine 5′-triphosphate disodium salt hydrate (ATP)	Sigma-Aldrich	Cat # A3377-10G

(*Continued on next page*)

Continued

REAGENT or RESOURCE	SOURCE	IDENTIFIER
Dithiothreitol (DTT)	Fisher Scientific	Cat # BP172-5
NP-40 (IGEPAL CA-630)	Sigma-Aldrich	Cat #I3021
Doxycycline	Sigma-Aldrich	Cat #D9891
Protease inhibitor cocktail	Roche	Cat # 11697498001
Freund's Complete Adjuvant	Millipore Sigma	Cat # 344289
Freund's Incomplete Adjuvant	Millipore Sigma	Cat # 344291
Puromycin dihydrochloride	Millipore Sigma	Cat #P8833
D-Luciferin potassium salt	Prolume	Cat # 306
Paraformaldehyde (PFA)	Electron Microscopy Sciences	Cat # 19200 CAS: 30525-89-4
LIVE/DEAD Fixable Aqua Vivid Cell Stain	Thermo Fisher Scientific	Cat # L34957
FreeStyle 293F expression medium	ThermoFisher Scientific	Cat # 12338002
ExpiFectamine 293 transfection reagent	ThermoFisher Scientific	Cat # A14525
Protein A Sepharose CL-4B	Cytiva	Cat # 17096303
Ni-NTA agarose	Invitrogen	Cat #R90110
Epitope Mapping Peptide Set SARS-CoV-2 (Spike Glycoprotein)	JPT Peptide Technologies	Cat # EMPS-WCPV-S-1
SARS-CoV-2 S2 26-mer (residue 1140–1165) (PLQPELDSFKEELD KYFKNHTSPDVD)	GenScript	N/A
Peptide #288 15-mer (KEELDKYFKNHTSPD)	GenScript	N/A
Peptide #289 15-mer (DKYFKNHTSPDVDLG)	GenScript	N/A
Peptide #289 11-mer (DKYFKNHTSPD)	GenScript	N/A
Peptide scramble 15-mer (DHDTKFLNYDPVGKS)	GenScript	N/A
Critical commercial assays		
PNGase F	New England BioLabs	Cat # P0704L
EXPRE^{35}S^{35}S Protein Labeling Mix (^{35}S-L-methionine, ^{35}S-L-cysteine)	PerkinElmer	Cat # NEG072007MC
QuikChange II XL Site-Directed Mutagenesis Kit	Agilent Technologies	Cat # #200522
Q5 Site-Directed Mutagenesis Kit	New England BioLabs	Cat # E0554S
iScript advanced cDNA kit	Bio Rad	Cat #1725038
Nano-Glo® Endurazine Live Cell Substrate™	Promega	Cat # N2571
Experimental models: Cell lines		
Vero E6 (female, Chlorocebus sabaeus)	ATCC	Cat # CRL-1586; RRID: CVCL_0574
HEK293T	ATCC	Cat # CRL-3216; RRID: CVCL_0063
293T-hACE2	Prévost et al. 2020	N/A
FreeStyle 293F cells	ThermoFisher Scientific	Cat # R79007; RRID: CVCL_D603
293T-S (Wuhan-Hu-1 strain)	Nguyen et al. 2021	N/A
Experimental models: Organisms/strains		
B6.Cg-Tg(K18-ACE2)2Prlmn/J	The Jackson Laboratory	Stock No: 034860 RRID:IMSR_JAX:034860
Recombinant DNA		
pCG1-SARS-CoV-2 Spike Wuhan-Hu-1	Hoffmann et al. 2020	N/A
pcDNA3.1-SARS-CoV-2 RBD	(Beaudoin-Bussières et al., 2020)	N/A
pCG1-SARS-CoV-2 Spike D614G	Beaudoin-Bussières et al., 2020	N/A

(*Continued on next page*)

Continued

REAGENT or RESOURCE	SOURCE	IDENTIFIER
pCG1-SARS-CoV-2 Spike Furin KO	This paper	N/A
pCG1-SARS-CoV-2 Spike B.1.429 variant	This paper	N/A
pcDNA3.1-SARS-CoV-2 Spike B.1.1.7 variant	Tauzin et al. 2021	N/A
pcDNA3.1-SARS-CoV-2 Spike B.1.351 variant	This paper	N/A
pcDNA3.1-SARS-CoV-2 Spike P.1 variant	This paper	N/A
pcDNA3.1-SARS-CoV-2 Spike B.1.526 variant	This paper	N/A
pCAGGS-SARS-CoV-2 Spike B.1.617.1 variant	This paper	N/A
pCAGGS-SARS-CoV-2 Spike B.1.617.2 variant	This paper	N/A
pNL4.3 R-E- Luc	NIH AIDS Reagent Program	Cat # 3418
pIRES2-eGFP vector	Clontech	Cat # 6029-1
pACP-tag(m)-2 ACE2-Fc fusion protein	Anand et al. 2020	N/A
pCMV-$S_{B.1.1.7}$	This Study	N/A
pCMV-$S_{B.1.1.7}$ Q3-1 A4-1	This Study	N/A
pCMV-$S_{B.1.1.7}$ d19	This Study	N/A
pCMV delta R8.2	Addgene	Cat #12263
pMX Puro PH-LgBiT	Yamamoto et al. 2019	N/A
pCAGGS-Cyclophilin A-HiBiT	This study	N/A
SARS-CoV-2 HexaPro-Spike (S-6P)	Hsieh et al. 2020	N/A
Software and algorithms		
Graphpad Prism v9.1.0	Graphpad	http://www.graphpad.com/ RRID:SCR_002798
FlowJo v10.5.3	Tree star	https://www.flowjo.com/ RRID:SCR_008520
cryoSPARC	Punjani et al. 2017; Rubinstein and Brubaker 2015	https://cryosparc.com/
COOT	Emsley and Cowtan, 2004	https://www2.mrc-lmb.cam.ac.uk/personal/pemsley/coot/
Phenix	Liebschner et al. 2019	https://phenix-online.org/
Pymol	Schrödinger	https://pymol.org/2/
SAbPred	Dunbar et al. 2016	http://opig.stats.ox.ac.uk/webapps/newsabdab/sabpred/
SerialEM software package	David N. Mastronarde, University of Colorado Boulder	https://bio3d.colorado.edu/SerialEM/ SCR_017,293
IMOD software package	David N. Mastronarde, University of Colorado Boulder	https://bio3d.colorado.edu/imod/ RRID: SCR_003297
Chimera	University of California, San Francisco	http://plato.cgl.ucsf.edu/chimera RRID: SCR_004097
ChimeraX	University of California, San Francisco	https://www.rbvi.ucsf.edu/chimerax/ RRID:SCR_015872
iMODFIT	Lopéz-Blanco and Chacón 2013	N/A
Protomo and I3	Winkler 2007	https://www.electrontomography.org/?page_id=446 RRID:SCR_017296
BioRender	BioRender.com	https://biorender.com/ RRID:SCR_018361

(*Continued on next page*)

Continued

REAGENT or RESOURCE	SOURCE	IDENTIFIER
Other		
TriStar LB 942 Multimode Microplate Reader and Luminometer	Berthold Technologies	N/A
BD LSR II Flow Cytometer	BD Biosciences	N/A
Maxisorp Nunc™ White 96-Well Flat-Bottom Microplate	ThermoFisher Scientific	Cat # 437796
Prism-based TIRF Microscope	Mothes Lab	N/A
C1000 Touch thermal cycler	Bio-Rad	N/A
FEI Titan Krios G2 300kV Transmission Electron Microscope	ThermoFisher Scientific	https://cryoem.yale.edu/equipment
Gravity-driven plunger apparatus	Mothes Lab	N/A
QUANTIFOIL® holey carbon grids	Electron Microscopy Sciences	Cat # Q250-CR1

RESOURCE AVAILABILITY

Lead contact

Further information and requests for resources and reagents should be directed to and will be fulfilled by the lead contact, Walther Mothes (walther.mothes@yale.edu).

Materials availability

All reagents generated in this study will be made available by the lead contact with a completed Materials Transfer Agreement.

Data and code availability

- The cryo-EM structures have been deposited to the Electron Microscopy Data Bank (EMDB). Cryo-ET structural maps for SARS-CoV-2 spike in complex with Fab CV3-1, the spike bound with Fab CV3-25 and the unliganded spike have been deposited in the EMDB with accession codes EMD-25564, EMD-25565 and EMD-25566, respectively. Cryo-EM structural map for Fab CV3-25 in complex with SARS-CoV-2 spike have been deposited in the EMDB with accession codes EMD-25200. The X-ray crystallography structure of Fab CV3-25 in complex with SARS-CoV-2 stem helix peptide has been deposited to the Protein Data Bank (RCSB PDB) under accession codes 7NAB.
- This paper does not report original code.
- Any additional information required to reanalyze the data in this paper is available from the lead contact upon request.

EXPERIMENTAL MODEL AND SUBJECT DETAILS

Cell lines

293T human embryonic kidney cells (ATCC) and 293T-ACE2 cells were maintained at 37°C under 5% CO_2 in Dulbecco's Modified Eagle Medium (DMEM) (Wisent), supplemented with 5% fetal bovine serum (FBS) (VWR) and 100 U/mL penicillin/streptomycin (Wisent). 293T-ACE2 cells stably expressing human ACE2 are derived from 293T cells and were maintained in medium supplemented with 2 μg/mL of puromycin (Millipore Sigma) (Prévost et al., 2020)

Antibodies

The human antibodies (CV3-1 and CV3-25) used in the work were isolated from the blood of convalescent donor S006 (male) recovered 41 days after symptoms onset using fluorescent recombinant stabilized Spike ectodomains (S2P) as probes to identify antigen-specific B cells as previously described (Jennewein et al., 2021). Site-directed mutagenesis was performed on plasmids expressing CV3-25 antibody heavy chain in order to introduce the GASDALIE mutations (G236A/S239D/A330L/I332E) using the QuickChange II XL site-directed mutagenesis protocol (Stratagene) (Ullah et al., 2021). Two New Zealand White rabbits were immunized with purified recombinant SARS-CoV-2 RBD proteins using MediMabs' 77-day Canadian Council on Animal Care (CCAC)-accredited protocol. Animals were hosted and handled at the CRCHUM Animal Facility and the experimental protocol received approval from the Institutional Animal Protection Committee prior the beginning of the manipulation (protocol #IP18039AFI). The first immunization was done using complete Freund's adjuvant (Millipore Sigma) followed by 4 immunizations with incomplete Freund's adjuvant (Millipore Sigma). Rabbits were used solely for this project and were sacrificed by total exsanguination. Blood was processed and serum was further used in immunoprecipitation experiments at 1:1000 dilution.

Mice

All experiments were approved by the Institutional Animal Care and Use Committees (IACUC) of and Institutional Biosafety Committee of Yale University (IBSCYU). All the animals were housed under specific pathogen-free conditions in the facilities provided and supported by Yale Animal Resources Center (YARC). hACE2 transgenic B6 mice (heterozygous) were obtained from Jackson Laboratory. 6–8-week-old male and female mice were used for all the experiments. The heterozygous mice were crossed and genotyped to select heterozygous mice for experiments by using the primer sets recommended by Jackson Laboratory.

METHOD DETAILS

Plasmids and site-directed mutagenesis

The plasmids expressing the wildtype SARS-CoV-2 Spike was previously reported (Hoffmann et al., 2020). The plasmid encoding for SARS-CoV-2 S RBD (residues 319–541) fused with a hexahistidine tag was previously described (Beaudoin-Bussières et al., 2020). The individual mutations in the full-length SARS-CoV-2 Spike expressor, the furin cleavage site mutations (R682S/R683S) and the Spike from the B.1.429 lineage (S13I, W152C, L452R, D614G) were generated using the QuikChange II XL site-directed mutagenesis kit (Agilent Technologies). The amino acid deletions in the full-length SARS-CoV-2 Spike expressor were generated using the Q5 site-directed mutagenesis kit (NEB). The presence of the desired mutations was determined by automated DNA sequencing. The plasmids encoding the Spike from the B.1.1.7 lineage (Δ69-70, Δ144, N501Y, A570D, D614G, P681H, T716I, S982A and D1118H), the B.1.351 lineage (L18F, D80A, D215G, Δ242–244, R246I, K417N, E484K, N501Y, D614G, A701V), the P.1 lineage (L18F, T20N, P26S, D138Y, R190S, K417T, E484K, N501Y, D614G, H655Y, T1027I) and the B.1.526 lineage (L5F, T95I, D253G, E484K, D614G, A701V) were codon-optimized and synthesized by Genscript. The plasmids encoding the Spike from the B.1.617.1 (E154K, L452R, E484Q, D614G, P681R) and the B.1.617.2 (T19R, Δ156–158, L452R, T478K, D614G, P681R, D950N) lineages were generated by overlapping PCR using a codon-optimized wild-type SARS-CoV-2 Spike gene that was synthesized (Biobasic, Markham, ON, Canada) and cloned in pCAGGS as a template. All constructs were validated by Sanger sequencing. The plasmid encoding for the ACE2-Fc chimeric protein, a protein composed of an ACE2 ectodomain (1–615) linked to an Fc segment of human IgG1 was previously reported (Anand et al., 2020).

Cryo-electron tomography sample preparation

Lentiviral particles were collected and clarified by low-speed spinning (1500g for 5 min) twice, then pelleted by ultracentrifugation (130,000g for 2 h) once and resuspended in PBS buffer. 6 nm gold tracer was added to the concentrated S-decorated HIV-1 lentivirus at 1:3 ratio, and 5 μL of the mixture was placed onto freshly glow discharged holey carbon grids (R 2/1, Quantifoil) for 1 min. Grids were blotted with filter paper, and plunge frozen into liquid ethane by a homemade gravity-driven plunger apparatus. Frozen grids were stored in liquid nitrogen until imaging.

Cryo-electron tomography data collection

Cryo-grids were imaged on a cryo-transmission electron microscope (Titan Krios, Thermo Fisher Scientific) operated at 300 kV, using a Gatan K3 direct electron detector in counting mode with a 20 eV energy slit. Tomographic tilt series between −60° and +60° were collected by using SerialEM (Mastronarde, 2005) in a dose-symmetric scheme (Hagen et al., 2017; Mastronarde and Held, 2017) with increments of 3°. The nominal magnification was 64,000×, giving a pixel size of 1.346 Å on the specimen. The raw images were collected from single-axis tilt series with accumulative dose of ∼120e per Å2. The defocus range was −2 to −6 μm and 9 frames were saved for each tilt angle. Detailed data acquisition parameters are summarized in Table S1.

Frames were motion-corrected using Motioncorr2 (Zheng et al., 2017) to generate drift-corrected stack files, which were aligned using gold fiducial makers by IMOD/etomo (Mastronarde and Held, 2017). The contrast transfer function (CTF) was measured by the ctfplotter package within IMOD. Tilt stacks were CTF-corrected by ctfphaseflip within IMOD. Tomograms were reconstructed by weighted back projection and tomographic slices were visualized with IMOD.

Cryo-electron tomography data analysis

For the CV3-1 sample, all spikes were manually picked. Euler angles were determined based on the vector between two points, one on the head of the spike and the other on the membrane where the spike locates. For CV3-25 and unliganded samples, a low-pass filtered (30Å) structure from previous aligned S structure was used as the template for template matching search in 8 x binned tomograms. Subtomograms were extracted for initial alignment. After this alignment, particles with cross-correlation coefficients (CCC) below 0.25 were removed. Visual inspection of the tomograms in IMOD confirmed that the rest of the subtomograms corresponded to S trimers on the viral surface. Particles that had tilted by more than 90° relative to their perpendicular positions to the viral surface were excluded. Subsequent processing was performed by using I3 (Winkler, 2007) with 2 x and 4 x binned tomograms.

All the density maps were segmented in the UCSF Chimera (Pettersen et al., 2004), and ChimeraX (Goddard et al., 2018; Pettersen et al., 2021) was used for surface rendering and visualization of cryo-ET maps and models. "Fit in map" tool in Chimera and ChimeraX was used for rigid fitting. iMODFIT was used for flexible fitting (Lopéz-Blanco and Chacón, 2013).

SARS-CoV-2 infection and treatment conditions

For all *in vivo* experiments, the 6 to 8 weeks male and female mice were intranasally challenged with 1 × 105 FFU in 25–30 μL volume under anesthesia (0.5–5% isoflurane delivered using precision Dräger vaporizer with oxygen flow rate of 1 L/min). For NAb treatment using prophylaxis regimen, mice were treated with 250 μg (12.5 mg/kg body weight) of indicated antibodies (CV3-1 or CV3-25 GASDALIE) via intraperitoneal injection (i.p.) 24 h prior to infection. The starting body weight was set to 100%. For survival experiments, mice were monitored every 6–12 h starting six days after virus administration. Lethargic and moribund mice or mice that had lost more than 20% of their body weight were sacrificed and considered to have succumbed to infection for Kaplan-Meier survival plots.

Focus forming assay

Titers of virus stocks was determined by standard plaque assay. Briefly, the 4 × 105 Vero-E6 cells were seeded on 12-well plate. 24 h later, the cells were infected with 200 μL of serially diluted virus stock. After 1 h, the cells were overlayed with 1mL of pre-warmed 0.6% Avicel (RC-581 FMC BioPolymer) made in complete RPMI medium. Plaques were resolved at 48 h post infection by fixing in 10% paraformaldehyde for 15 min followed by staining for 1 h with 0.2% crystal violet made in 20% ethanol. Plates were rinsed in water to visualize plaques.

Measurement of viral burden

Indicated organs (nasal cavity, brain, lungs from infected or uninfected mice were collected, weighed, and homogenized in 1 mL of serum free RPMI media containing penicillin-streptomycin and homogenized in 2 mL tube containing 1.5 mm Zirconium beads with BeadBug 6 homogenizer (Benchmark Scientific, TEquipment Inc). Virus titers were measured using three highly correlative methods. Frist, the total RNA was extracted from homogenized tissues using RNeasy plus Mini kit (Qiagen Cat # 74136), reverse transcribed with iScript advanced cDNA kit (Bio-Rad Cat #1725036) followed by a SYBR Green Real-time PCR assay for determining copies of SARS-CoV-2 N gene RNA using primers SARS-CoV-2 N F: 5′'-ATGCTGCAATCGTGCTACAA-3′' and SARS-CoV-2 N R: 5′-GACTGCCGCCTCTGCTC-3′.

Second, serially diluted clarified tissue homogenates were used to infect Vero-E6 cell culture monolayer. The titers per milligram of tissue were quantified using standard plaque forming assay described above.

Analyses of signature inflammatory cytokines mRNA

Brain and lung samples were collected from mice at the time of necropsy. Approximately, 20 mg of tissue was suspended in 500 μL of RLT lysis buffer, and RNA was extracted using RNeasy plus Mini kit (Qiagen Cat # 74136), reverse transcribed with iScript advanced cDNA kit (Bio-Rad Cat #1725036). To determine levels of signature inflammatory cytokines, multiplex qPCR was conducted using iQ Multiplex Powermix (Bio Rad Cat # 1725848) and PrimePCR Probe Assay mouse primers FAM-GAPDH, HEX-IL6, TEX615-CCL2, Cy5-CXCL10, and Cy5.5-IFNgamma. The reaction plate was analyzed using CFX96 touch real time PCR detection system. Scan mode was set to all channels. The PCR conditions were 95°C 2 min, 40 cycles of 95°C for 10 s and 60°C for 45 s, followed by a melting curve analysis to ensure that each primer pair resulted in amplification of a single PCR product. mRNA levels of Il6, Ccl2, Cxcl10 and Ifng in the cDNA samples of infected mice were normalized to Gapdh with the formula ΔCt(target gene) = Ct(target gene)-Ct(Gapdh). The fold increase was determined using 2-ΔΔCt method comparing treated mice to uninfected controls.

Virus-cell fusion inhibition assay

The split nanoluc assay was used to measure antibody-mediated inhibition of virus-cell fusion (Yamamoto et al., 2019; Lu et al., 2020). Pseudoviruses decorated with SARS-CoV-2 Spike were prepared by transfecting HEK293T cells (70% confluent 10 cm dishes) with a plasmid mixture of 5 μg of psPAX2 (Gag-pol, Rev, and Tat expression vector; does not express Vpr), 5 μg of pCMV-d19 Spike (last 19 residues at C-terminal were deleted) from the B.1.1.7 variant or WH01 G614, and 2 μg of a pCAGGS-Cyclophilin A-HiBiT construct using polyetherimide (PEI). Two days post transfection, virus containing supernatants were clarified using a 0.45 μM PDVF filter (Pall Corp, NY, USA # 4614) and pelleted by ultracentrifugation on a 15% sucrose cushion before resuspension in culture media to achieve a 20X concentration over the original volume. Freshly prepared viruses were incubated for 2 h at 37°C with triplicate, 10-fold serial dilutions of CV3-25 antibody or non-specific IgG (Jackson Immunoresearch, PA, USA # 305-005-003) in a white, flat bottom 96 well plate (Greiner Bio-One, NC, USA # 655083).

HEK293T-ACE2 target cells were transfected in a 24 well plate using PEI with 500ng/well of pMX Puro PH-LgBiT (LgBiT-tagged to pleckstrin homology domain of human phospholipase Cδ the N terminus, Yamamoto et al., 2019). 1 day post transfection, cells were resuspended at 2×10^6 cells/ml in culture media containing Nano-Glo® Endurazine Live Cell Substrate™ (Promega Inc, WI, USA # N2571) and DrkBiT (Promega Inc, WI, USA # CS3002A01) according to the manufacturer's recommended concentrations and incubated for 2 h at 37°C. Labeled target cells were passed through a 70 μM cell strainer and added to the virus + antibody dilution plate (10^5 cells/well). The assay plate was then incubated for 1 h at 37°C before measuring luminescence with a Tristar multiwell luminometer (Berthold Technology, Bad Wildbad, Germany). %RLU was calculated by normalizing RLU values to wells without virus (min) and wells without antibody (max).

smFRET imaging of S on SARS-CoV-2 VLPs

Lentiviruses carrying SARS-CoV-2 spikes were prepared similarly as previously described (Lu et al., 2020). Two short peptides labeling tags (Q3: GQQQLG; A4: DSLDMLEM) were introduced into designed positions in the S1 subunit on the plasmid encoding SB.1.1.7, pCMV-SB.1.1.7. Plasmids pCMV-SB.1.1.7, dual-tagged pCMV-SB.1.1.7 Q3-1 A4-1, and pCMV delta R8.2 were transfected into 293T cells at a ratio of 20:1:21. Using this very diluted ratio of tagged-S vs. wildtype S, for the virus particles containing tagged S, more than 95% S trimers will have one dual-tagged protomer and two wildtype protomers within a trimer. Using this strategy, we generated lentiviral particles with an average of one dual-tagged S protomer for conjugating FRET-paired fluorophores among predominantly wildtype S trimers presented on lentivirus surface. Viral particles were harvested 40 h post-transfection, filtered with a 0.45 μm pore size filter, and partially purified using ultra-centrifugation at 25,000 rpm for 2 h through a 15% sucrose cushion made in PBS. Then the particles were re-suspended in 50 mM pH 7.5 HEPES buffer, labeled with self-healing Cy3 and Cy5 derivatives (LD555-CDand LD650-CoA, respectively) and purified through an OptiprepTM (Sigma Aldrich) gradient as previously described (Lu et al., 2019, 2020; Munro et al., 2014). smFRET images of viral particles was acquired on a home-built prism-based total internal reflection fluorescence (TIRF) microscope, as described previously (Lu et al., 2020). The conformational effects of 50 μg/mL CV3-1 and CV3-25 antibodies on SARS-CoV-2 spike were tested by pre-incubating fluorescently labeled viruses for 60 min at 37°C before imaging in the continued presence of the antibodies. Signals were simultaneously recorded on two synchronized ORCA-Flash4.0 V3 sCMOS cameras (Hamamatsu) at 25 frames per second for 80 s smFRET data analysis was performed using MATLAB (MathWorks)-based customized SPARTAN software package (Juette et al., 2016). Each FRET histogram was fitted into the sum of four Gaussian distributions in Matlab, where each Gaussian distribution represents one conformation and the area under each Gaussian curve estimates the occupancy of each state.

Recombinant protein expression and purification

FreeStyle 293-F (Thermo Fisher) cells were grown to a density of 1×10^6 cells/mL at 37°C with 8% CO2 with regular 135 rpm agitation. A plasmid encoding for non-cleavable, pre-fusion-stabilized SARS-CoV-2 S ectodomain (1–1208) (HexaPro, S-6P [Hsieh et al., 2020; Wrapp et al., 2020]-a gift from Dr. Jason S. McLellan) with a removable C-terminal twin-strep tag was transfected into cells with EndoFectin Max (GeneCopoeia) using the manufacturer's protocol. One-week post-transfection, the clarified supernatant was purified on strep-tactin resin (IBA) followed by size-exclusion chromatography on a Superose 6 10/300 column (GE Healthcare) equilibrated with 10 mM Tris-HCl pH 8.0 and 200 mM NaCl as the running buffer (SEC buffer). The C-terminal twin-Strep-Tag was removed by HRV3C (Sigma Aldrich) digestion overnight at 4°C and the uncleaved protein was removed by passage over Ni-NTA resin. The cleaved protein was further purified on a Superose 6 10/300 column in SEC buffer. Alternatively, cells were transfected with a plasmid coding for SARS-CoV-2 RBD or ACE2-Fc and were purified on Ni-NTA resin (Invitrogen) or Protein A resin (Cytiva), respectively. Protein purity was confirmed by SDS-PAGE. Only freshly isolated protein was used for Cryo-EM grid preparations.

Expression plasmids encoding the heavy and light chains of CV3-1 IgG or CV3-25 IgG were transiently transfected into Expi293F cells (Thermo Fisher) with ExpiFectamine 293 transfection reagent using the manufacturer's protocol (Thermo Fisher). After 6-days post transfection, antibody was purified on Protein A resin from cell supernatant (Thermo Fisher). Fab was generated by overnight papain digestion at 37°C using immobilized papain agarose (Thermo Fisher). Fab was separated from Fc and uncleaved IgG by passage over protein A resin followed by size-exclusion chromatography on a Superose 6 10/300 column before being used in SPR binding, X-Ray crystallography or Cryo-EM experiments.

Surface plasmon resonance

All surface plasma resonance assays were performed on a Biacore 3000 (GE Healthcare) with a running buffer of 10 mM HEPES pH 7.5 and 150 mM NaCl supplemented with 0.05% Tween 20 at 25°C. Initial peptide scanning was performed by the binding of a series of SARS-CoV-2 S2 synthetic peptides (GenScript) to immobilized CV3-25 IgG (~5800 RU) on a Protein A sensor chip (Cytiva). For the kinetic binding measurements of S2 peptides #289 (15-mer), #289 (11-mer) and the 26mer (1140–1165) to CV3-25, ~5800 RU of CV3-25 IgG was first immobilized on a protein A chip (Cytiva) and 2-fold serial dilutions of the S2 peptides were then injected with concentrations ranging from 6.25 to 200 nM. After each cycle the protein A sensor chip was regenerated with 0.1 M Glycine pH 2.0. CV3-1 IgG was used as a negative control. All sensorgrams were corrected by subtraction of the corresponding blank channel in addition to the buffer background and the kinetic constant determined using a 1:1 Langmuir model with the BIAevaluation software (GE Healthcare). Goodness of fit of the curve was evaluated by the Chi2 value with a value below 3 considered acceptable.

Cryo-EM sample preparation and data collection

The purified non-tagged SARS-CoV-2 HexaPro spike (293F produced) was incubated with 20-fold excess of CV3-25 Fab overnight at 4°C before purification on a Superose 6 300/10 GL column (GE Healthcare). The complex peak was harvested, concentrated to about 0.5 mg/mL in SEC buffer and immediately used for CryoEM grid preparation. 3 μL of protein was deposited on a holey copper grids (QUANTIFOIL R 1.2/1.3, 200 mesh, EMS) which had been glow-discharged for 30s at 15 mA (Tedpella Inc). The grids were vitrified in liquid ethane using a Vitrobot Mark IV (Thermo Fisher) with a blot time of 2–4 s and the blot force of 20 at 4°C and 95% humidity.

Cryo-EM data from a good grid were acquired in 300kV Titan Krios electron microscope, equipped with a Gatan K2-BioQuantum Image filter camera system (Thermo Fisher and Gatan Inc.) in National Cancer Institute/NIH IRP cryoEM facility,

Bethesda MD. 50-frame image stacks were collected at a magnification of 165,000x, corresponding to a calibrated pixel size of 0.821 Å/pixel, with a total exposure dose of 59.3 e^-/Å from 5s exposure.

CryoEM data processing, model building and analysis

Motion correction, CTF estimation, particle picking, curation and extraction, 2D classification, ab initio model reconstruction, volume refinements and local resolution estimation were carried out in cryoSPARC (Punjani et al., 2017; Rubinstein and Brubaker, 2015). An initial SARS-CoV-2 spike model (PDB: 6XKL [Hsieh et al., 2020]) with single-RBD up was used as a modeling template. The NTDs were initially modeled from PDB entry 7LY3(McCallum et al., 2021). The initial docking model for CV3-25 Fab was taken from the crystallography model in this study.

Automated and manual model refinements were iteratively carried out in ccpEM (Burnley et al., 2017), Phenix (real-space refinement) (Liebschner et al., 2019) and Coot(Emsley and Cowtan, 2004). Geometry validation and structure quality evaluation were performed by EM-Ringer (Barad et al., 2015) and Molprobity (Chen et al., 2010). Model-to-map fitting cross correlation and figures generation were carried out in USCF Chimera, Chimera X (Goddard et al., 2018; Pettersen et al., 2004, 2021) and PyMOL (The PyMOL Molecular Graphics System, Version 2.0 Schrödinger, LLC.). The complete cryoEM data processing workflow is shown in Figure S2 and statistics of data collection, reconstruction and refinement is described in Table S3.

Crystallization and structure determination of CV3-25 with S2 stem peptide

CV3-25 Fab was prepared and purified as described (Ullah et al., 2021). 10 mg/mL of CV3-25 was mixed with synthetic S2 peptide spanning residues 1153–1163, 1153–1167 or 1140–1165 (26mer) in a 1:10 molar ratio of Fab to peptide. Crystal screening of Fab-peptide complexes were performed using the vapor-diffusion hanging drop method using the sparse matrix crystallization screens ProPlex (Molecular Dimensions), Index (Hampton Research), or Crystal Screen I and II (Hampton Research) with a 1:1 ratio of protein to well solution. After approximately 2 weeks incubation at 21°C, diffraction-quality co-crystals of the Fab-26mer were obtained in 0.1 M sodium citrate pH 5.6, 20% PEG4000 and 20% isopropanol. Crystals were snap-frozen in the crystallization condition supplemented with 20% 2-methyl-2, 4-pentanediol (MPD) as the cryoprotectant. X-ray diffraction data were collected at the SSRL beamline 9-2 and was processed with HKL3000 (Minor et al., 2006). The structure was solved by molecular replacement in Phenix (Liebschner et al., 2019) using a CV3-25 framework model generated by SAbPred (Dunbar et al., 2016). Iterative cycles of model building and refinement were done in Coot (Emsley and Cowtan, 2004) and Phenix. Structural analysis and figure generation were performed in PyMOL and ChimeraX. Fab-peptide interface and buried surface area were determined in PISA (Krissinel and Henrick, 2007). Data collection and refinement statistics are shown in Table S2.

Flow cytometry analysis of cell-surface staining

Using the standard calcium phosphate method, 10 μg of Spike expressor and 2 μg of a green fluorescent protein (GFP) expressor (pIRES2-eGFP; Clontech) was transfected into 2 × 10^6 293T cells. At 48h post transfection, 293T cells were stained with anti-Spike monoclonal antibodies CV3-25, CV3-1 (5 μg/mL) or using the ACE2-Fc chimeric protein (20 μg/mL) for 45 min at 37°C. Alternatively, to determine the Hill coefficients (Anand et al., 2020), cells were preincubated with increasing concentrations of CV3-25 or CV3-1 (0.04–20 μg/mL). Alexa Fluor-647-conjugated goat anti-human IgG (H + L) Abs (Invitrogen) were used as secondary antibodies to stain cells for 30 min at room temperature. The percentage of transfected cells (GFP + cells) was determined by gating the living cell population based on the basis of viability dye staining (Aqua Vivid, Invitrogen). Samples were acquired on an LSRII cytometer (BD Biosciences) and data analysis was performed using FlowJo v10.5.3 (Tree Star). Hill coefficient analyses were done using GraphPad Prism version 9.1.0 (GraphPad). Alternatively, for peptide epitope competition assay, CV3-25 (5μg/mL) was pre-incubated in presence of increasing concentrations of peptide #288 (1149-KEELDKYFKNHTSPD-1163), peptide #289 (1153-DKYFKNHTSPDVDLG-1167), a shorter version of peptide #289 (1153-DKYFKNHTSPD-1163) or a scramble version of the peptide #289 (DHDTKFLNYDPVGKS), which were synthesized by Genscript.

Viral neutralization assay

293T-ACE2 target cells were infected with single-round luciferase-expressing lentiviral particles (Prévost et al., 2020). Briefly, 293T cells were transfected by the calcium phosphate method with the lentiviral vector pNL4.3 R-E− Luc (NIH AIDS Reagent Program) and a plasmid encoding for SARS-CoV-2 Spike at a ratio of 5:4. Two days post-transfection, cell supernatants were harvested and stored at −80°C until further use. 293T-ACE2 target cells were seeded at a density of 1×10^4 cells/well in 96-well luminometer-compatible tissue culture plates (PerkinElmer) 24h before infection. To measure virus neutralization, recombinant viruses in a final volume of 100 μL were incubated with increasing concentrations of CV3-1 or CV3-25 (0.01–10 μg/mL) for 1h at 37°C and were then added to the target cells followed by incubation for 48h at 37°C; cells were lysed by the addition of 30 μL of passive lysis buffer (Promega) followed by one freeze-thaw cycle. An LB942 TriStar luminometer (Berthold Technologies) was used to measure the luciferase activity of each well after the addition of 100 μL of luciferin buffer (15 mM $MgSO_4$, 15 mM KH_2PO_4 [pH 7.8], 1 mM ATP, and 1 mM dithiothreitol) and 50 μL of 1 mM D-luciferin potassium salt (Prolume). The neutralization half-maximal inhibitory dilution (IC_{50}) represents the antibody concentration inhibiting 50% of the infection of 293T-ACE2 cells by recombinant viruses bearing the indicated surface glycoproteins. Alternatively, for peptide epitope competition assay, CV3-25 (10 μg/mL) was pre-incubated in presence of increasing concentrations of peptide #289 (1153-DKYFKNHTSPDVDLG-1167) or a scramble version of the same peptide (DHDTKFLNYDPVGKS).

Radioactive labeling and immunoprecipitation

For pulse-labeling experiments, 5×10^5 293T cells were transfected by the calcium phosphate method with SARS-CoV-2 Spike expressors. One day after transfection, cells were metabolically labeled for 16 h with 100 μCi/mL [^{35}S]methionine-cysteine ([^{35}S] protein labeling mix; PerkinElmer) in Dulbecco's modified Eagle's medium lacking methionine and cysteine and supplemented with 10% of dialyzed fetal bovine serum and 1X GlutaMAX™ (ThermoFisher Scientific). Cells were subsequently lysed in radioimmunoprecipitation assay (RIPA) buffer (140 mM NaCl, 8 mM Na_2HPO_4, 2 mM NaH_2PO_4, 1% NP-40, 0.05% sodium dodecyl sulfate [SDS], 1.2mM sodium deoxycholate [DOC]) with protease inhibitors (ThermoFisher Scientific). Precipitation of radiolabeled SARS-CoV-2 Spike glycoproteins from cell lysates or supernatant was performed with CV3-25 in combination with a polyclonal rabbit antiserum raised against SARS-CoV-2 RBD protein for 1 h at 4°C in the presence of 45 μL of 10% protein A-Sepharose beads (GE Healthcare).

Peptide scanning ELISA

SARS-CoV-2 Spike peptide ELISA (enzyme-linked immunosorbent assay) The SARS-CoV-2 Spike ELISA assay used was adapted from a previously described ELISA (Prévost et al., 2020). Peptides covering the entire SARS-CoV-2 S2 sequence with a length of 15 residues (15-mer) and an overhang of 4 residues were purchased from JPT Peptide Technologies. Briefly, SARS-CoV-2 S2 peptide pools or individual peptides (1 μg/mL), or bovine serum albumin (BSA) (1 μg/mL) as a negative control, were prepared in PBS and were adsorbed to plates (MaxiSorp; Nunc) overnight at 4°C. Coated wells were subsequently blocked with blocking buffer (Tris-buffered saline [TBS] containing 0.1% Tween 20 and 2% BSA) for 1 h at room temperature. Wells were then washed four times with washing buffer (TBS containing 0.1% Tween 20). CV3-25 mAb (50 ng/mL) was prepared in a diluted solution of blocking buffer (0.1% BSA) and incubated with the peptide-coated wells for 90 min at room temperature. Plates were washed four times with washing buffer followed by incubation with HRP-conjugated anti-IgG secondary Abs (Invitrogen) (diluted in a diluted solution of blocking buffer [0.4% BSA]) for 1 h at room temperature, followed by four washes. HRP enzyme activity was determined after the addition of a 1:1 mix of Western Lightning oxidizing and luminol reagents (PerkinElmer Life Sciences). Light emission was measured with an LB942 TriStar luminomete (Berthold Technologies). Signal obtained with BSA was subtracted for each plate.

Western blotting

293T-S cells express the wild-type S glycoprotein from a SARS-CoV-2 Wuhan-Hu-1 strain (Nguyen et al., 2021). 293T-S cells were seeded in 6-well plates at a density of 1×10^6 cells per well on day 0. On day 1, cells were either induced with 1 μg/mL doxycycline or mock treated as a control. Two days after induction, cells were lysed with lysis buffer (1x PBS, 1% NP-40, 1x protease inhibitor cocktail [Roche]). Cell lysates were subjected to Western blotting using the CV3-1 or CV3-25 antibodies; mouse anti-S1 antibody (Sino Biological) and rabbit anti-S2 antibody (Sino Biological) were used as controls. The Western blots were developed with horseradish peroxidase (HRP)-conjugated secondary antibodies (anti-human IgG, anti-mouse IgG or anti-rabbit IgG, correspondingly). To evaluate antibody recognition of S glycoproteins lacking N-linked glycans, 293T-S cells expressing the wild-type SARS-CoV-2 S glycoprotein were lysed with lysis buffer, as described above. Lysates were treated with PNGase F (NEB) following the manufacturer's instructions or mock treated as a control. The lysates were then Western blotted with the CV3-25 antibody, as described above.

QUANTIFICATION AND STATISTICAL ANALYSIS

Data were analyzed and plotted using GraphPad Prism software (La Jolla, CA, USA). Statistical significance for pairwise comparisons were derived by applying non-parametric Mann-Whitney test (two-tailed). To obtain statistical significance for survival curves, grouped data were compared by log rank (Mantel-Cox) test. To obtain statistical significance for grouped data we employed one-way ANOVA with a Holm-Sidak post-test (Figures 1A and 1B, 3F and 3G) or 2-way ANOVA followed by Tukey's multiple comparison tests (Figure 1D).p values lower than 0.05 were considered statistically significant. P values were indicated as *, $p < 0.05$; **, $p < 0.01$; ***, $p < 0.001$; ****, $p < 0.0001$.

Schematics

Schematics for showing experimental design in figures were created with BioRender.com.